Steady-state solutions in a nonlinear pool boiling model

Michel Speetjens[*], Arnold Reusken[*], Wolfgang Marquardt[†]

RWTH Aachen, Templergraben 55, D-52056 Aachen, Germany.

Abstract

We consider a relatively simple model for pool boiling processes. This model involves only the temperature distribution within the heater and desribes the heat exchange with the boiling fluid via a nonlinear boundary condition imposed on the fluid-heater interface. This results in a standard heat equation with a nonlinear Neumann boundary condition on part of the boundary. In this paper we analyze the qualitative structure of stationary solutions of this heat equation. It turns out that depending the model allows both multiple homogeneous and multiple heterogeneous solutions in certain regimes of the parameter space. The latter solutions originate from bifurcations on a certain branch of homogeneous solutions. We present a bifurcation analysis that reveals the multiple solution structure in this mathematical model. In the numerical analysis a continuation algorithm is combined with the method of separation-of-variables and a Fourier collocation technique. For both, the continuous and discrete problem a fundamental symmetry property is derived that implies multiplicity of heterogeneous solutions. It will be shown that numerical simulations for this model problem predict phenomena that are consistent with laboratory observations for pool boiling processes.

AMS subject classification. 35K55, 65P30, 80A20, 93A30

Keywords. pool boiling, nonlinear heat transfer, bifurcation analysis, numerical simulation

1 Introduction

Pool boiling refers to boiling processes that lean on natural convection as a means for heat transfer between a heater surface and the boiling fluid; it is the key mode of thermal transport in many practical applications. Local heat transfer phenomena near heating walls in industrial boiling equipment (e.g. evaporators and kettle reboilers) for instance are essentially pool boiling processes (see e.g. Thome (2003)). Furthermore, pool boiling is emerging as novel cooling technique for electronics components (see e.g. Mudawar (2001)). Despite its importance, many aspects of (pool) boiling remain largely unexplored to date, mainly due to the immense complexity of the process emanating from the intricate interplay between fluid

[*]Chair of Numerical Analysis
[†]Chair of Process Systems Engineering

dynamics, heat transfer from the heater to the fluid and phase transfer. Studies on boiling known in the literature are mainly experimental and empirical. Numerical studies based on a model of reasonable degree of detail are numerous but theoretical investigations aiming at a rigorous analysis of such models are scarce. The theoretical analysis of a simple boiling model presented in this paper is intended to contribute to a better qualitative understanding of fundamental phenomena in pool boiling.

In pool boiling there are three fundamental boiling modes – namely nucleate, transition and film boiling – that occur successively with increasing temperature (see Dhir (1998)). Nucleate boiling is, as opposed to film boiling, an efficient and safe mode of heat transfer; it is the desired boiling mode in most practical applications. Nucleate boiling transits into film boiling upon exceeding the so-called critical heat flux (CHF) through the intermediate state of transition boiling. This transition results in a dramatic increase in interface temperature due to the substantial drop in the heat transfer coefficient when going from nucleate boiling (homogeneous liquid-like mixture) to film boiling (vapour blanket on the interface). This manifests itself in the essentially nonlinear relation between the mean heat flux and the mean interface temperature (the so-called boiling curve; see Dhir (1998)) which results from averaging over the heater surface of the experiment and over the measurement time interval. The improvement of the efficiency of boiling processes involves finding a good balance between high heat transfer coefficients (close to CHF) and low risk (safe distance from CHF). In-depth understanding of transition boiling and its underlying mechanisms is imperative to achieve such a balance (see e.g. Theofanous *et al.* (2002)).

Transition boiling has been interpreted as a boiling mode with coexisting nucleate boiling and film boiling regions ("two-mode boiling"') and thus resulting essentially in a heterogeneous state at the surface (see e.g. Dhir (1991)). A more intricate and most likely more precise description of the two-phase structure in transition boiling has been derived in a series of papers by Auracher and co-workers (see Auracher & Marquardt (2004) for a survey). Moreover, transition boiling is an inherently unstable state that naturally evolves towards one of the two stable boiling modes, i.e. to nucleate or film boiling, unless actively stabilised through temperature control (see Auracher & Marquardt (2002)). On mesoscopic length and time scales two-mode boiling states correspond to heterogeneous temperature fields on the interface: "lower" temperatures correspond to nucleate boiling regions; "higher" temperatures are associated with film boiling regions.[1] Furthermore, the propagation of boundaries between adjacent boiling regions during evolution of the transition mode towards one of the stable modes is consistent with the propagation of thermal waves at the fluid-heater interface (see e.g. Zhukov *et al.* (1980), Blum *et al.* (1999)). This phenomenological connection between a (mesoscopic) boiling mode and interface temperature admits a heater-only modelling approach that leaves out the boiling fluid and describes the (qualitative) behaviour of the boiling system entirely in terms of the temperature distribution within the heater. The heat exchange between the heater and the fluid is modelled by a nonlinear heat flux relation that is similar to the boiling curve Blum *et al.* (1999). The simplification from the multi-phase problem to a heater-only model naturally disqualifies this approach for detailed quantitative studies. However, the heater-only approach allows the analysis of fundamental (mesoscopic) boiling phenomena using numerical analysis.

This approach has found widespread application for the analysis of pool boiling on "thin"

[1]Here mesoscopic means locally averaged in space and time over intervals larger than bubble dimensions and bubble lifetimes in order to smooth out microscopic short-term fluctuations (see van Ouwekerk (1972)).

heaters such as wires and foils (cf. Gabaraev *et al.* (2001), Kovalev (1966), Kovalev & Rybchinskaya (1978), Kovalev & Usitakov (2003), Zhukov *et al.* (1980), Zhukov & Barelko (1983)). In such thin configurations the heat flux relation results in a nonlinear source term in the heat governing equations that thus these are very similar to reaction-diffusion systems (see e.g. Blum *et al.* (1999)) and generic current-carrying systems (see Gurevich & Mints (1987)). First extensions to finite-thickness heaters, where the heat flux relation leads to a nonlinear boundary condition and thus an essentially different heat transfer model, are presented in Blum *et al.* (1999).

The transition behaviour of the heater-only problem basically involves two issues: (i) formation and (ii) dynamics of heterogeneous temperature fields (see Auracher & Marquardt (2004)). These two issues lead to questions concerning existence and stability of steady-state solutions. Analysis of thin heaters has shown the existence of *multiple* steady-state solutions for given heating conditions. Each set of steady-state solutions turns out to contain at most two stable solutions; other solutions are unstable (see e.g. Kovalev & Usitakov (2003)). Results obtained for cylindrical heaters with linearised heat flux relations are consistent with these results (see Blum *et al.* (1998)). However, similar studies on thick heaters for the generic case of nonlinear heat flux relations and heterogeneous interface temperatures are restricted to the analysis of Blum *et al.* (1999). The latter contains a numerical study of the evolution of two-mode boiling states towards one of the two stable boiling modes (i.e nucleate- or film boiling) on a 2D thick heater. Initial two-mode boiling states (unstable steady states) are represented by discontinuous – and thus rather artificial – temperature profiles, though. Numerical studies which show the existence of realistic *heterogeneous steady-state solutions* are not known to the authors.

In this paper we present an extensive analysis of the steady-state behaviour of a spatially two-dimensional (2D) thick heater problem. The heat transfer model that we use is similar to the one introduced by Blum *et al.* (1999). We show that multiple steady-state solutions occur in this model for specific experimental conditions. A main topic is the analysis of the dependence of the multiple solution structure on the system parameters. To this end a bifurcation analysis of the governing mathematical model is performed in order to identify solution branches and bifurcations as a function of the system parameters. This analysis is based on a numerical continuation algorithm combined with the method of separation-of-variables and a Fourier collocation method for the governing heat equation.

The paper is organised as follows. In Section 2 we present the model problem. Basic properties of this continuous model are derived in Section 3. In Section 4 the discretization method and the continuation algorithm are explained. In Section 5 we apply these methods to a representative case study. In Section 6 a comprehensive bifurcation analysis of the system is presented. A few main conclusions are summarised in Section 7.

2 Problem definition and mathematical model

2.1 Dimensional heater-only model

Our pool boiling investigations are based on the heater-only modelling approach introduced in Section 1 and following Blum *et al.* (1999). We consider the two-dimensional rectangular heater $\mathcal{D} = [0, L] \times [0, H]$, with boundary $\Gamma = \partial\mathcal{D} = \Gamma_H \cup \Gamma_A \cup \Gamma_F$. The boundary segments are $\Gamma_H = \{(x, y) \in \mathcal{D} \mid y = 0\}$ (heat supply), $\Gamma_A = \{(x, y) \in \mathcal{D} \mid x = 0 \text{ or } x = L\}$ (adiabatic sidewalls) and $\Gamma_F = \{(x, y) \in \mathcal{D} \mid y = H\}$ (fluid-heater interface), cf. Figure 1*a*. The heat

transfer is described in terms of the superheat $T = T_a - T_S$, i.e. the temperature difference between the actual temperature T_a of the heater and the boiling temperature T_S of the fluid. The temperature distribution $T(\boldsymbol{x}, t)$ in $\mathcal{D} \times [0, t_{\text{end}}]$ is modelled by the heat equation

$$\frac{\partial T}{\partial t} = \alpha \Delta T \qquad \text{in } \mathcal{D} \times [0, t_{\text{end}}], \quad \alpha = \frac{\lambda}{\rho c_p}, \tag{1}$$

$$-\lambda \frac{\partial T}{\partial n}|_{\Gamma_H} = q_H, \quad -\lambda \frac{\partial T}{\partial n}|_{\Gamma_F} = q_F(T_F), \quad \frac{\partial T}{\partial n}|_{\Gamma_A} = 0, \tag{2}$$

$$T(\boldsymbol{x}, 0) = T_0(\boldsymbol{x}) \qquad \text{for } \boldsymbol{x} \in \mathcal{D}, \tag{3}$$

where T_F denotes the interface temperature on the boundary segment Γ_F. The constants ρ, c_p and λ are density, specific heat and thermal conductivity of the heater and α the corresponding thermal diffusivity; q_H and q_F represent the (spatio-temporally constant) heat supply and temperature-dependent heat transfer to the boiling fluid, respectively.

Closure of the heat transfer model requires specification of the heat flux function $q_F(T_F)$. The boiling curve is not guaranteed to hold locally on the heater surface at any particular point in time since it is obtained from experiments which average over time and space in a certain experimental situation. However, if we pragmatically assume that either liquid or vapor is in contact with a certain point on the surface at a certain time, the local heat transfer model is supposed to reflect heat transfer correlations specific to liquid contact below some threshold of the local heater surface temperature and specific to vapor contact above this threshold. Since discontinuous heat transfer correlations will not occur in practice, the discontinuity between these two heat transfer modes will be mollified by some smooth transition. For simplicity, we identify $q_F(T_F)$ with the functional form of the global boiling curve. Such boiling curves are of the functional form sketched in Figure 1*b*. They consist of three distinct regimes, of which each corresponds to one of the boiling modes: nucleate boiling ($0 \leq T \leq T_C$), transition boiling ($T_C < T < T_M$) and film boiling ($T \geq T_M$). The nucleate and film boiling regions refer to local liquid and vapor contacts respectively, while the film boiling region represents the mollification of the discontinuity. Temperatures T_C and T_M coincide with the local maximum (Q_C; CHF of the boiling curve) and the local minimum (Q_M; Leidenfrost point of the boiling curve) heat fluxes, respectively, and T_D is a typical temperature in the mollification region (or during transition boiling). An explicit expression for the relation $q_F(T_F)$ that we use is given below.

2.2 Non-dimensional formulation

We formulate the heat transfer problem (1)-(3) in non-dimensional form through rescaling of the relevant variables according to $\boldsymbol{x}' = \boldsymbol{x}/L$, $T' = T/T_D$, $t' = t/\tau$, $q'_H = q_H/Q_H$ and $q'_F = q_F/Q_H$. The quantity Q_H is a typical value for the heat supply. Substitution into the governing equations and dropping primes yields the non-dimensional model

$$\begin{aligned} &\frac{\partial T}{\partial t} = \kappa \Delta T \qquad \text{in } \mathcal{D} \times [0, t_{\text{end}}/\tau] \ , \quad \mathcal{D} := [0,1] \times [0, D], \\ &-\Lambda \frac{\partial T}{\partial y}|_{\Gamma_H} = 1, \quad -\Lambda \frac{\partial T}{\partial y}|_{\Gamma_F} = \Pi_2 \, q_F(T_F), \quad \frac{\partial T}{\partial n}|_{\Gamma_A} = 0, \\ &T(\boldsymbol{x}, 0) = T_0(\boldsymbol{x}) \qquad \text{for } \boldsymbol{x} \in \mathcal{D}, \end{aligned} \tag{4}$$

with non-dimensional parameters

$$\Lambda = \frac{\lambda T_D}{Q_H L}, \quad \kappa = \frac{\lambda \tau}{\rho c_p L^2}, \quad D = \frac{H}{L}, \quad \Pi_1 = \frac{Q_C}{Q_M}, \quad \Pi_2 = \frac{Q_C}{Q_H}, \quad \Pi_3 = \frac{T_C}{T_M}. \tag{5}$$

Note that $q_F(T_F)$ is the normalised boiling curve; the dimensionless interfacial heat flux is given by $\Pi_2 q_F(T_F)$. Figure 2 shows the non-dimensional heater configuration (panel *a*) and the corresponding normalised boiling curve $q_F(T_F)$ (panel *b*). Physical considerations suggest $\tau = \rho c_p H T_D / |Q_H - Q_C|$ and lead to $\Lambda D/\kappa = |1 - \Pi_2|$. Thus the model contains five independent system parameters. Parameters Λ and κ are the non-dimensional thermal conductivity and thermal diffusivity, respectively, and thus determine the thermal properties of the heater; parameter Π_2 is the non-dimensional CHF, or alternatively, its reciprocal can be interpreted as the non-dimensional heat supply; hence Π_2 controls the heating conditions.

The normalised boiling curve can be parametrized by

$$q_F(T_F) = h(T_F) T_F, \tag{6}$$

with a temperature-dependent heat transfer coefficient $h(T_F)$,

$$h(T_F) := C_D \left\{ F_1 - F_2 H(C_D T_F - 1) \right\}, \quad H(x) = \frac{1}{2} \left[\tanh\left(\frac{2x}{W}\right) + 1 \right], \tag{7}$$

where $H(x)$ is a smoothed version of the Heaviside function. The parameter W sets the width of the transition region (from $H = 0$ to $H = 1$) around $x = 0$ and is specified *a-priori*. The coefficient C_D rescales the temperature such that the single deflection point of $q_F(T_F)$ coincides with $T_F = 1$. Its value is defined implicitly through

$$2\frac{dH}{dT}(C_D - 1) + \frac{d^2H}{dT^2}(C_D - 1) = 0,$$

and thus depends only on W. The coefficients F_1 and F_2 scale $q_F(T_F)$ such that the conditions

$$\dot{q}_F(T_{max}) = 0, \quad \dot{q}_F(T_{min}) = 0, \quad q_F(T_{max}) = 1, \quad q_F(T_{min}) = \Pi_1^{-1}, \tag{8}$$

are fulfilled, i.e. the extrema of the normalised boiling curve are consistent with their dimensional counterparts, where $\dot{q}_F = dq_F/dT$. These conditions result for given W and Π_1 in four nonlinear equations for the four unknowns $(F_1, F_2, T_{min}, T_{max})$. (It can be shown that q_F according to (7) possesses a local maximum and minimum at $T_{max} < 1$ and $T_{min} > 1$, respectively.) The temperatures $T_{max}, 1, T_{min}$ are the non-dimensional counterparts to T_C, T_D, T_M; the heat fluxes $q_F = 1$ and $q_F = \Pi_1^{-1}$ are the normalised counterparts to the critical heat flux (Q_C) and the Leidenfrost heat flux (Q_M), respectively. Figure 2*b* shows the boiling curve thus attained for $W = 1$ and $\Pi_1 = 4$. Note that W indirectly sets Π_3; both parameters may therefore be used interchangeably without loss of generality. The present boiling curve is a generalisation of that proposed by Blum *et al.* (1999) in that here the transition width W is an additional system parameter. For $W \downarrow 0$ we obtain the boiling curve used by Blum *et al.* (1999).

3 Analysis of the steady-state problem

We study the *steady-state* behaviour of the 2D nonlinear heat transfer problem introduced in Section 2. Similar to the thin counterparts, the model (4)-(7) is expected to admit multiple

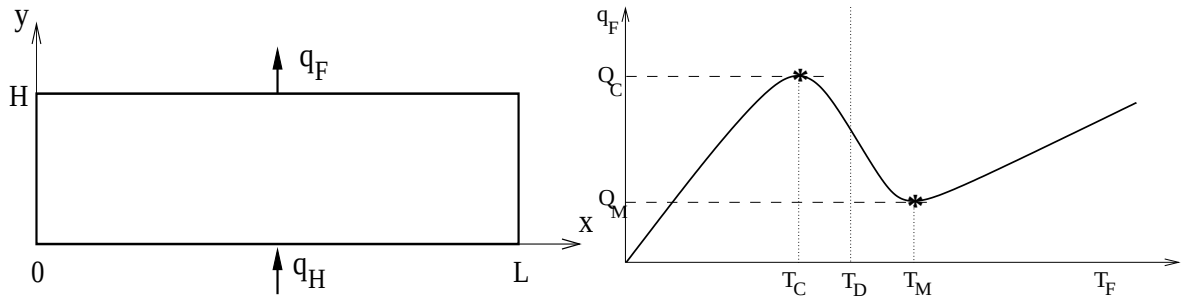

a) Heater configuration. *b) Boiling curve.*

Figure 1: *Heater configuration (panel a) and boiling curve (panel b). Temperatures T_C and T_M coincide with the local maximum (Q_C; CHF) and local minimum (Q_M; Leidenfrost point) heat fluxes, respectively; T_D is a typical temperature during transition boiling.*

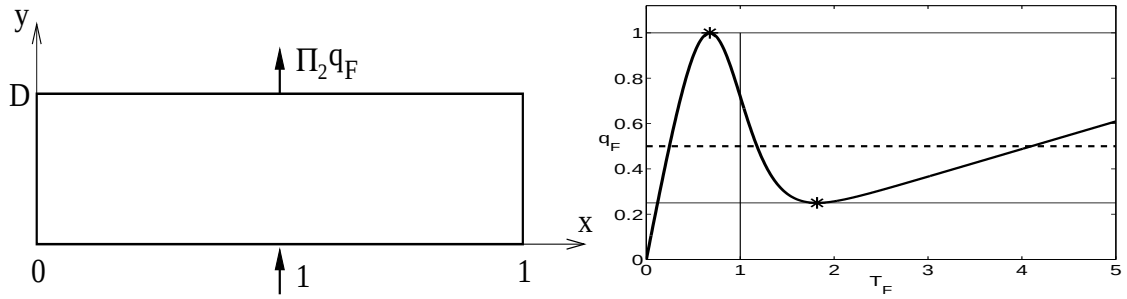

a) Heater configuration. *b) Boiling curve.*

Figure 2: *Non-dimensional model: heater configuration (panel a) and normalised boiling curve for $\Pi_1 = 4$ and $W = 1$ (panel b). $T = 1$ is the non-dimensional counterpart of T_D; the local maximum and minimum (stars) are the normalised CHF ($q_F = 1$) and Leidenfrost points ($q_F = \Pi_1^{-1}$), respectively. The dashed line represents the normalised heat supply $q_H^* = \Pi_2^{-1}$.*

steady-state solutions. For an analysis of this conjecture we consider the corresponding steady-state heat transfer problem

$$\begin{aligned} \Delta T = 0 \qquad & \text{in } \ \mathcal{D} = [0,1] \times [0,D], \\ -\Lambda \frac{\partial T}{\partial y}|_{\Gamma_H} = 1, \qquad & -\Lambda \frac{\partial T}{\partial y}|_{\Gamma_F} = \Pi_2 \, q_F(T_F), \qquad \frac{\partial T}{\partial n}|_{\Gamma_A} = 0, \end{aligned} \tag{9}$$

with the associated set of parameters $(\Lambda, D, \Pi_1, \Pi_2, W)$. We apply the method of separation-of-variables (see e.g. Kreyszig (1999)) to derive a (formal) representation of the solution of the Laplace equation and the linear Neumann boundary conditions on Γ_H and Γ_A in (9). This results in

$$T(x,y) = \sum_{n=0}^{\infty} \widetilde{T}_n \frac{\cosh(n\pi y)}{\cosh(n\pi D)} \cos(n\pi x) + \frac{D-y}{\Lambda}, \tag{10}$$

which can easily be checked by substitution. The coefficients $\widetilde{T}_n$ form the spectrum of the Fourier cosine expansion

$$T_F(x) := T(x,D) = \sum_{n=0}^{\infty} \widetilde{T}_n \cos(n\pi x) \tag{11}$$

of the fluid-heater interface temperature. The coefficients $\widetilde{T}_n$ are determined by the nonlinear Neumann boundary condition on Γ_F . Substitution of (10) into the nonlinear boundary condition in (9) and using (6) leads to

$$\sum_{n=0}^{\infty} n\pi \tanh(n\pi D)\widetilde{T}_n \cos(n\pi x) + \alpha(T_F(x))T_F(x) - \frac{1}{\Lambda} = 0 \quad \text{for all} \;\; x \in [0,1], \tag{12}$$

where

$$\alpha(T_F) = \frac{\Pi_2}{\Lambda} h(T_F) = \frac{\Pi_2}{\Lambda} \frac{q_F(T_F)}{T_F}$$

is the scaled heat transfer coefficient. The nonlinear equation (12) is the characteristic equation that determines the particular properties of the steady-state solutions to (9). The series in (11) and (12) are formal expressions. Convergence of these series is discussed below.

Thus the 2D steady-state problem (9) *simplifies to the 1D problem* (12) *involving only the temperature profile* $T_F(x)$ *on the boundary* Γ_F.

We first consider the special case of *spatially homogeneous* interface temperatures T_F, implying $T_F(x) = \widetilde{T}_0$ and $\widetilde{T}_n = 0$ for $n > 0$. Then the nonlinear condition (12) simplifies to

$$q_F(\widetilde{T}_0) = \Pi_2^{-1} \tag{13}$$

and $\widetilde{T}_0$ coincide(s) with the intersection(s) between the boiling curve (solid line in Figure 2*b*) and the normalised heat supply $q_H^* = \Pi_2^{-1}$ (dashed line in Figure 2*b*). From Figure 2*b* it follows that, depending on the system parameters, we can have one, two or three solutions for $\widetilde{T}_0$. Note that the heat transfer coefficient $h(T_F)$ is constant in this homogeneous case and thus that the Neumann boundary condition on Γ_F is linear. The corresponding solution in $\mathcal{D}$ is given by

$$T(x,y) = \frac{D}{\Lambda}\left(1 - \frac{y}{D}\right) + \widetilde{T}_0 \;, \tag{14}$$

which is a linear temperature profile with the constant interface temperature $T_F(x) = \widetilde{T}_0$ defined by (13).

We now return to the general case and derive two properties, that play an important role in the remainder of this paper. We first introduce the Fourier space of *convergent* Fourier cosine series

$$V_k := \{\, g : \mathbb{R} \to \mathbb{R} \mid g(x) = \sum_{n=0}^{\infty} a_{kn} \cos(kn\pi x) \quad \forall\, x \in \mathbb{R} \,\}, \quad k = 1, 2, \ldots \tag{15}$$

Functions from this space are $\frac{2}{k}$-periodic and even (i.e. $g(x) = g(-x)$). Such functions are uniquely determined by their values at $x \in [0, \frac{1}{k}]$. For the Fourier coefficients a_{kn} we have the representation

$$a_0 = \int_0^1 g(x)\, dx, \quad a_{kn} = 2\int_0^1 g(x)\cos(kn\pi x)\, dx \;\; (kn > 0).$$

Note that $V_{k+1} \subset V_k$ for all k. The Fourier transform on V_1 is denoted by $\mathcal{F} : V_1 \to \ell^2$:

$$\text{for } \; g(x) = \sum_{n=0}^{\infty} a_n \cos(n\pi x), \quad \mathcal{F}(g) := (a_n)_{n\geq 0}.$$

For $(b_n)_{n\geq 0}$, $(c_n)_{n\geq 0} \in \ell^2$ we define the product $(b_n)_{n\geq 0} \cdot (c_n)_{n\geq 0} := (b_n c_n)_{n\geq 0}$, i.e., element-wise multiplication of the entries in the sequences. In view of (12) we introduce the sequence $\mathbf{d} = (d_n)_{n\geq 0}$ defined by

$$d_n := n\pi \tanh(n\pi D) \quad \text{for all } \; n.$$

To guarantee that the expressions on the left handside in (12) are well-defined we only consider functions from the following subset of V_1:

$$S := \{\, g \in V_1 \mid \mathbf{d} \cdot \mathcal{F}(g) \in \text{range}(\mathcal{F}) \;\text{ and }\; (\alpha \circ g)g \in V_1 \,\}.$$

Remark 1 Functions $g \in V_1$ that are *sufficiently smooth* are elements of S. We do not study this smoothness issue here, but only give one simple result related to this. Elementary Fourier analysis yields that if $g \in V_1$ and $g \in C^3(\mathbb{R})$ then $g \in S$ holds.

The operator on the left handside in (12) has the following form

$$\mathcal{G}(T_F) := \mathcal{F}^{-1}\big(\mathbf{d} \cdot \mathcal{F}(T_F)\big) + (\alpha \circ T_F)T_F - \frac{1}{\Lambda}, \quad \text{for } \; T_F \in S. \tag{16}$$

From the definition of S it immediately follows that $\mathcal{G} : S \to V_1$. Thus (12) leads to the following problem:

$$\text{Determine } T_F \in S, \text{ such that } \quad \mathcal{G}(T_F) = 0\,. \tag{17}$$

The operator $\mathcal{G}$, defined on S, is (strongly) nonlinear. The homogeneous solutions given by (13) satisfy $\mathcal{G}(\widetilde{T}_0) = 0$.We now show that for every $k \geq 1$ the range of $\mathcal{G}_{|V_k}$ is contained in V_k.

Theorem 1 *The following holds:*

$$\mathcal{G} : V_k \cap S \to V_k \quad \textit{for all } \; k \geq 1.$$

Proof. For $k = 1$ this is trivial due to the definition of S. Take $T_F \in V_k \cap S$. Then T_F can be represented as $T_F(x) = \sum_{n=0}^{\infty} \widetilde{T}_{kn} \cos(kn\pi x)$ and all Fourier coefficients $\widetilde{T}_m$ with $m \bmod k \neq 0$ are equal to zero. We obtain

$$\begin{aligned}
\mathcal{G}(T_F)(x) &= \sum_{n=0}^{\infty} d_n \widetilde{T}_n \cos(n\pi x) + \alpha(T_F(x))T_F(x) - \frac{1}{\Lambda} \\
&= \sum_{n=0}^{\infty} d_{kn} \widetilde{T}_{kn} \cos(kn\pi x) + \alpha(T_F(x))T_F(x) - \frac{1}{\Lambda} \\
&=: w_1(x) + w_2(x) - \frac{1}{\Lambda}.
\end{aligned}$$

From $T_F \in S$ it follows that the series $w_1(x) = \sum_{n=0}^{\infty} d_{kn} \widetilde{T}_{kn} \cos(kn\pi x)$ converges and thus $w_1 \in V_k$. From $T_F \in S$ it also follows that $w_2 = (\alpha \circ T_F)T_F \in V_1$ and thus w_2 has a convergent cosine Fourier series. Furthermore, because T_F is $\frac{2}{k}$-periodic and even it follows that w_2 is $\frac{2}{k}$-periodic and even, and thus $w_2 \in V_k$. Hence, we have $\mathcal{G}(T_F) = w_1 + w_2 - \frac{1}{\Lambda} \in V_k$. $\square$

In the next theorem we present a symmetry property of heterogeneous solutions.

Theorem 2 *Assume that there exists $k \geq 1$ and $T_F \in V_k \cap S$ such that $T_F \notin V_\ell$ for $\ell > k$ and*

$$T_F(x) = \sum_{n=0}^{\infty} \widetilde{T}_{kn} \cos(kn\pi x) \tag{18}$$

satisfies $\mathcal{G}(T_F) = 0$. Define

$$T_F^*(x) := T_F(x + \frac{1}{k}) = \sum_{n=0}^{\infty} \widetilde{T}_{kn}^* \cos(kn\pi x), \quad \textit{with} \;\; \widetilde{T}_{kn}^* = (-1)^n \widetilde{T}_{kn}. \tag{19}$$

Then $T_F^* \in V_k \cap S$ satisfies $\mathcal{G}(T_F^*) = 0$, and $T_F^* \neq T_F$.

Proof. Since $T_F \in V_k \cap S$ is even and $\frac{2}{k}$-periodic and T_F^* is a translation of T_F by $\frac{1}{k}$ it follows that $T_F^* \in V_k \cap S$. Using

$$T_F(x + \frac{1}{k}) = \sum_{n=0}^{\infty} \widetilde{T}_{kn} \cos(kn\pi(x + \frac{1}{k})) = \sum_{n=0}^{\infty} (-1)^n \widetilde{T}_{kn} \cos(kn\pi x)$$

we obtain the representation in (19). Note that

$$T_F(x) - T_F^*(x) = \sum_{n=0}^{\infty} (1 - (-1)^n) \widetilde{T}_{kn} \cos(kn\pi x).$$

Assume that $T_F = T_F^*$ holds. Then $\widetilde{T}_{kn} = 0$ must hold for all odd n, and thus we obtain the representation $T_F(x) = \sum_{n=0}^{\infty} \widetilde{T}_{2kn} \cos(2kn\pi x)$. This implies $T_F \in V_{2k}$, which contradicts the assumption $T_F \notin V_\ell$ for $\ell > k$. Thus $T_F^* \neq T_F$ must hold. For arbitrary $x \in \mathbb{R}$ we have

$$\begin{aligned}
\mathcal{G}(T_F^*)(x) &= \mathcal{F}^{-1}\big(\mathbf{d} \cdot \mathcal{F}(T_F^*)\big)(x) + \alpha(T_F^*(x)) T_F^*(x) \\
&= \sum_{n=0}^{\infty} d_{kn} (-1)^n \widetilde{T}_{kn} \cos(kn\pi x) + \alpha(T_F(x + \frac{1}{k})) T_F(x + \frac{1}{k}) \\
&= \sum_{n=0}^{\infty} d_{kn} \widetilde{T}_{kn} \cos(kn\pi(x + \frac{1}{k})) + \alpha(T_F(x + \frac{1}{k})) T_F(x + \frac{1}{k}) \\
&= \mathcal{F}^{-1}\big(\mathbf{d} \cdot \mathcal{F}(T_F)\big)(x + \frac{1}{k}) + \alpha(T_F(x + \frac{1}{k})) T_F(x + \frac{1}{k}) \\
&= \mathcal{G}(T_F)(x + \frac{1}{k}) = 0.
\end{aligned}$$

Hence, $\mathcal{G}(T_F^*) = 0$ holds. □

This result shows that heterogeneous solutions in $V_1 \cap S$, if they exist, always occur as a conjugate pair: (18) and (19). (Note that the dual solution T_F^* is obtained from T_F by a translation with half the period of T_F.) This implies a fundamental non-uniqueness in the steady states under heterogeneous boiling conditions, consistent with laboratory experiments (see e.g. Auracher & Marquardt (2004)).

In the proof of Theorem 2 we derived the following fundamental property of the operator $\mathcal{G}$. Let $s_k : \mathbb{R} \to \mathbb{R}$ be the linear shift function $s_k(x) := x + \frac{1}{k}$. For $T_F \in V_k \cap S$ the relation

$$\mathcal{G}(T_F \circ s_k) = s_k \circ \mathcal{G}(T_F) \tag{20}$$

holds. Due to this commutator property of the nonlinear operator $\mathcal{G}$ and the linear shift operator s_k we obtain the symmetry result in Theorem 2.

Remark 2 In the proofs of Theorem 1 and Theorem 2 we did not use any specific information about the form of the function $\alpha(\cdot)$. Hence these results hold for an arbitrary (smooth) boiling curve q_F.

4 Numerical solution method

The steady-state solutions are obtained by solving the characteristic equation (12). For homogeneous solutions the latter simplifies to (13) which can easily be solved by a standard root-finding algorithm. Hence, homogeneous solution branches are easily identified. Heterogeneous solutions, however, have to be determined via a discretisation and continuation approach that is explained in this section. Numerical results obtained with this method will be presented in Sections 5 and 6.

4.1 Discretisation method

Discretisation of (12) is based on a standard Fourier collocation method (see Canuto *et al.* (1987)). We briefly review a few basic facts from discrete Fourier analysis. Consider for $N \in \mathbb{N}$ the equidistant mesh $x_j = j/N,\ j \in \mathbb{N}$. The discrete Fourier cosine transform of an even 2-periodic function $u(x) = u(x+2)$ is given by

$$\sum_{n=0}^{N} \widetilde{u}_n \cos(n\pi x), \quad \widetilde{u}_n := \frac{c_n}{N}\left\{ u(0) + 2\sum_{j=1}^{N-1} u(x_j)\cos(n\pi x_j) + (-1)^n u(1) \right\}, \tag{21}$$

with $c_0 = c_N = 1/2$ and $c_n = 1$ otherwise. This function satisfies

$$\sum_{n=0}^{N} \widetilde{u}_n \cos(n\pi x_i) = u(x_i) \quad \text{for all} \ \ 0 \le i \le N.$$

Hence, the (physical) values $\boldsymbol{u} = (u_0, \ldots, u_N)^T$, with $u_j := u(x_j)$, relate to the spectral coefficients $\widetilde{\boldsymbol{u}} = (\widetilde{u}_0, \ldots, \widetilde{u}_N)^T$ via

$$\boldsymbol{u} = \boldsymbol{V}\widetilde{\boldsymbol{u}}, \quad , \quad \boldsymbol{V} := \begin{bmatrix} 1 & \cos(\pi x_0) & \ldots & \cos(N\pi x_0) \\ \vdots & \vdots & & \vdots \\ 1 & \cos(\pi x_N) & \ldots & \cos(N\pi x_N) \end{bmatrix}. \tag{22}$$

An elementary computation yields

$$(\boldsymbol{V}\boldsymbol{D})^{-1} = \frac{2}{N}\,\boldsymbol{V}\boldsymbol{D}, \quad \text{with} \ \ \boldsymbol{D} = \begin{bmatrix} 1/2 & & & & \\ & 1 & & & \\ & & \ddots & & \\ & & & 1 & \\ & & & & 1/2 \end{bmatrix}. \tag{23}$$

The discretisation of (12) is as follows: determine $T_F(x_j) = \sum_{n=0}^{N} \widetilde{T}_n \cos(n\pi x_j),\ 0 \le j \le N$, such that

$$\sum_{n=0}^{N} d_n \widetilde{T}_n \cos(n\pi x_j) + \alpha(T_F(x_j))T_F(x_j) - \frac{1}{\Lambda} = 0 \quad \text{for all} \ \ 0 \le j \le N. \tag{24}$$

This set of $N+1$ (nonlinear) equations for the unknowns $\widetilde{T}_n$ $(0 \le n \le N)$ or, equivalently, $T_F(x_j)$ $(0 \le j \le N)$, can be represented in a compact matrix-vector formulation. We use the notation $T_j := T_F(x_j)$ $(j = 0, \ldots, N)$, $\boldsymbol{t} = (T_0, \ldots, T_N)^T$ and $\tilde{\boldsymbol{t}} = (\widetilde{T}_0, \ldots, \widetilde{T}_N)^T$. Note that $\boldsymbol{t}$ consists of the discrete temperature values on the boundary Γ_F and $\tilde{\boldsymbol{t}}$ contains the corresponding Fourier coefficients. We introduce the diagonal matrices

$$\boldsymbol{K}_S = \mathrm{diag}(d_n)_{0 \le n \le N} \ , \quad \boldsymbol{M}(\boldsymbol{t}) = \mathrm{diag}\big(\alpha(T_j)\big)_{0 \le j \le N} \ ,$$

the vector $\boldsymbol{g} = (1/\Lambda, \ldots, 1/\Lambda)^T$ and the matrix $\boldsymbol{K} := \boldsymbol{V}\boldsymbol{K}_S\boldsymbol{V}^{-1}$. Then the discrete problem (24) can be formulated as follows: determine $\boldsymbol{t} \in \mathbb{R}^{N+1}$ such that

$$\boldsymbol{\mathcal{G}}(\boldsymbol{t}) := \big(\boldsymbol{K} + \boldsymbol{M}(\boldsymbol{t})\big)\boldsymbol{t} - \boldsymbol{g} = 0. \tag{25}$$

The above defines a nonlinear system in the (physical) unknown $\boldsymbol{t}$. The equivalent representation in the (spectral) unknown $\tilde{\boldsymbol{t}}$ is given by

$$\big(\boldsymbol{K}_S + \boldsymbol{M}_S(\tilde{\boldsymbol{t}})\big)\tilde{\boldsymbol{t}} = \boldsymbol{V}^{-1}\boldsymbol{g} \ , \quad \boldsymbol{M}_S(\tilde{\boldsymbol{t}}) := \boldsymbol{V}^{-1}\boldsymbol{M}(\boldsymbol{V}\tilde{\boldsymbol{t}})\boldsymbol{V}. \tag{26}$$

The nonlinearity of the problems (25) and (26) is contained in the *diagonal* matrix $\boldsymbol{M}(\boldsymbol{t})$ and the *full* matrix $\boldsymbol{M}_S(\tilde{\boldsymbol{t}})$, respectively. The former admits a more efficient numerical treatment and thus we have used the physical representation (25) in our numerical simulations.

For the discrete nonlinear operator $\boldsymbol{\mathcal{G}} : \mathbb{R}^{N+1} \to \mathbb{R}^{N+1}$ in (25) we will derive properties similar to those for the continuous operator $\mathcal{G}$ in the Theorems 1 and 2. For this we first introduce some further notation. Let $\mathbf{v}_m$ be the m-th column of the matrix $\mathbf{V}$ in (22). Define

$$V_k^N := \mathrm{span}\{\, \mathbf{v}_{kn} \mid 0 \le n \le \frac{N}{k} \,\}, \quad k = 1, \ldots, N.$$

This space is the discrete analogon of V_k in (15). Note that $V_k^N \subset V_1^N = \mathbb{R}^{N+1}$ for all k. We now derive a discrete analogon of Theorem 1. For this we need the following lemma.

Lemma 1 *Let $1 \le k \le N$ be such that $N \bmod k = 0$. For $\boldsymbol{t} \in V_k^N$ we then have $M(\boldsymbol{t})\boldsymbol{t} \in V_k^N$.*

Proof. Define $m := \frac{N}{k}$. For a vector $\boldsymbol{z} \in \mathbb{R}^{N+1}$ we use the notation $\boldsymbol{z} = (z_0, z_1, \ldots, z_N)^T$. For $\boldsymbol{t} \in V_k^N$ we have $\boldsymbol{t} = \sum_{n=0}^m \alpha_n \mathbf{v}_{kn}$ and thus $t_i = \sum_{n=0}^m \alpha_n \cos(kn\pi x_i)$ for $0 \le i \le N$. From this it follows that

$$t_{m+i} = t_{m-i} \ \ (0 \le i \le m), \quad t_{i+2m} = t_i \ \ (0 \le i \le N - 2m).$$

The vector $\boldsymbol{r} := M(\boldsymbol{t})\boldsymbol{t}$ has entries $r_i = \alpha(t_i)t_i$ and thus we have

$$r_{m+i} = r_{m-i} \ \ (0 \le i \le m), \quad r_{i+2m} = r_i \ \ (0 \le i \le N - 2m). \tag{27}$$

The vector $(r_j)_{0 \le j \le m}$ has a Fourier transform, cf. (21),

$$\begin{aligned} r_j &= \sum_{\ell=0}^m \tilde{r}_\ell \cos(\ell\pi\hat{x}_j) \quad (\hat{x}_j := \frac{j}{m}) \\ &= \sum_{\ell=0}^m \tilde{r}_\ell \cos(k\ell\pi x_j), \quad 0 \le j \le m. \end{aligned}$$

Due to (27) and $\cos(k\ell\pi x_{m+j}) = \cos(k\ell\pi x_{m-j})$ $(0 \le j \le m)$, $\cos(k\ell\pi x_{j+2m}) = \cos(k\ell\pi x_j)$ $(0 \le j \le N-2m)$ we obtain

$$r_j = \sum_{\ell=0}^{m} \tilde{r}_\ell \cos(k\ell\pi x_j) \quad \text{for all} \;\; 0 \le j \le N.$$

Hence, $\boldsymbol{r} = \sum_{\ell=0}^{m} \tilde{r}_\ell \boldsymbol{v}_{k\ell}$, i.e., $\boldsymbol{r} \in V_k^N$ holds. □

Theorem 3 *Let $1 \le k \le N$ be such that $N \bmod k = 0$. The following holds:*

$$\boldsymbol{\mathcal{G}} : V_k^N \to V_k^N. \tag{28}$$

Proof. The operator $\boldsymbol{\mathcal{G}} : V_1^N \to V_1^N$ is defined by $\boldsymbol{\mathcal{G}}(\boldsymbol{t}) = \boldsymbol{K}\boldsymbol{t} + \boldsymbol{M}(\boldsymbol{t})\boldsymbol{t} - \boldsymbol{g}$. For $\boldsymbol{t} \in V_k^N$ we have $\boldsymbol{M}(\boldsymbol{t})\boldsymbol{t} \in V_k^N$ due to Lemma 1. Note that $\boldsymbol{g} \in V_k^N$ for all k and N. We now consider the term $\boldsymbol{K}\boldsymbol{t} = \boldsymbol{V}\boldsymbol{K}_S\boldsymbol{V}^{-1}\boldsymbol{t}$ with $\boldsymbol{K}_S = \mathrm{diag}(d_n)_{0 \le n \le N}$. For $\boldsymbol{t} \in V_k^N$, with $m := \frac{N}{k}$, we have $\boldsymbol{t} = \sum_{n=0}^{m} \alpha_{kn} \boldsymbol{v}_{kn}$. Thus

$$\boldsymbol{V}\boldsymbol{K}_S\boldsymbol{V}^{-1}\boldsymbol{t} = \sum_{n=0}^{m} d_{kn}\alpha_{kn}\boldsymbol{v}_{kn}$$

holds. This yields $\boldsymbol{K}\boldsymbol{t} \in V_k^N$ and completes the proof. □

The symmetry property for the continuous problem as formulated in Theorem 2 is inherited by the discretisation. We formulate a discrete analogon of Theorem 2:

Theorem 4 *Let $1 \le k \le N$ be such that $N \bmod k = 0$ and define $m := \frac{N}{k}$. Assume that there exists $\boldsymbol{t} = \sum_{n=0}^{m} \tilde{t}_{kn}\boldsymbol{v}_{kn} \in V_k^N$ such that $\boldsymbol{t} \notin V_\ell^N$ for $\ell > k$ and $\boldsymbol{\mathcal{G}}(\boldsymbol{t}) = 0$. Define*

$$\boldsymbol{t}^* = \sum_{n=0}^{m} (-1)^n \tilde{t}_{kn}\boldsymbol{v}_{kn}. \tag{29}$$

Then $\boldsymbol{t}^* \in V_k^N$ satisfies $\boldsymbol{\mathcal{G}}(\boldsymbol{t}^*) = 0$, and $\boldsymbol{t}^* \neq \boldsymbol{t}$.

Proof. Assume that $\boldsymbol{t} = \boldsymbol{t}^*$. Then $\sum_{n=0}^{m}(1-(-1)^n)\tilde{t}_{kn}\boldsymbol{v}_{kn} = 0$ and thus $\tilde{t}_{kn} = 0$ for all odd n. This yields $\boldsymbol{t} = \sum_{n=0}^{[\frac{1}{2}m]} \tilde{t}_{2kn}\boldsymbol{v}_{2kn}$, i.e., $\boldsymbol{t} \in V_{2k}^N$, which contradicts the assumption $\boldsymbol{t} \notin V_\ell^N$ for $\ell > k$. Thus $\boldsymbol{t} \neq \boldsymbol{t}^*$.
From

$$\begin{aligned} t_j &= \sum_{n=0}^{m} \tilde{t}_{kn} \cos(kn\pi x_j) \\ t_j^* &= \sum_{n=0}^{m} \tilde{t}_{kn} \cos(kn\pi(x_j + \frac{1}{k})) = \sum_{n=0}^{m} \tilde{t}_{kn} \cos(kn\pi x_{j+m}), \end{aligned}$$

for $0 \le j \le N$, it follows that

$$\begin{aligned} t_j^* &= t_{j+m} \quad \text{for} \;\; 0 \le j \le N-m \\ t_j^* &= t_{2N-m-j} \quad \text{for} \;\; N-m \le j \le N. \end{aligned} \tag{30}$$

From

$$\boldsymbol{\mathcal{G}}(\boldsymbol{t})_j = \sum_{n=0}^{m} d_{kn}\tilde{t}_{kn}\cos(kn\pi x_j) + \alpha(t_j)t_j - \frac{1}{\Lambda}$$
$$\boldsymbol{\mathcal{G}}(\boldsymbol{t}^*)_j = \sum_{n=0}^{m} d_{kn}\tilde{t}_{kn}\cos(kn\pi x_{j+m}) + \alpha(t^*_j)t^*_j - \frac{1}{\Lambda},$$

for $0 \le j \le N$, and (30) it follows that

$$\begin{aligned} \boldsymbol{\mathcal{G}}(\boldsymbol{t}^*)_j &= \boldsymbol{\mathcal{G}}(\boldsymbol{t})_{j+m} \quad \text{for} \;\; 0 \le j \le N-m \\ \boldsymbol{\mathcal{G}}(\boldsymbol{t}^*)_j &= \boldsymbol{\mathcal{G}}(\boldsymbol{t})_{2N-m-j} \quad \text{for} \;\; N-m \le j \le N. \end{aligned} \tag{31}$$

Since $\boldsymbol{\mathcal{G}}(\boldsymbol{t})_j = 0$ for all $0 \le j \le N$ we obtain $\boldsymbol{\mathcal{G}}(\boldsymbol{t}^*) = 0$. □

The result in this theorem shows that if a discrete heterogeneous solution $\boldsymbol{t} \in V_k^N$ exists, then the "shifted" vector $\boldsymbol{t}^* \in V_k^N$ as in (30) also satisfies the discrete equations. The results in (30) and (31) form the discrete analogon of the commutator property in (20).

We note that the assumption $N \bmod k = 0$ used in the Theorems 3 and 4 is not very restrictive. Firstly note that it is fulfilled for $k = 1$. Assume that we have a discrete solution $\boldsymbol{t} \in V_k^N$ with $k > 1$ and $N = N_0$. This solution $\boldsymbol{t} = \boldsymbol{t}(N_0)$ is only of interest if it is a member of a sequence $(\boldsymbol{t}(N))_{N \ge N_0}$ of discrete solutions with $\boldsymbol{t}(N) \in V_k^N$ and $\boldsymbol{t}(N)$ converges for $N \to \infty$ (i.e., in the process of repeated grid refinement) to a continuous heterogenous solution $T_F \in V_k$. It is no strong restriction to consider only mesh sizes such that N is an integer multiple of k.

Remark 3 Related to the discrete problem the same comment as in Remark 2 holds. The results in the Theorems 3 and 4 do not depend on the specific form of the function $\alpha(\cdot)$.

4.2 Continuation strategy

For solving the discrete nonlinear system (25) we apply a continuation method. The nonlinearity in the model is caused by the nonlinear boundary heat flux condition

$$q_F(T_F) = C_D\left\{F_1 - F_2 H(C_D T_F - 1)\right\} T_F$$

with coefficients C_D, F_1, F_2 and a Heaviside function $H(\cdot)$ as explained in Section 2.2. The model is linear if q_F is a linear function of T_F. This motivates our choice of an additional non-physical parameter, P, which is well suited for continuation from the linear to the nonlinear regime. We define

$$q_F(T_F, P) := C_D\left\{F_1 - PF_2 H(C_D T_F - 1)\right\} T_F, \quad \text{for} \;\; 0 \le P \le 1. \tag{32}$$

For $P = 0$ we have a linear boundary condition; for $P = 1$ the original nonlinear condition is recovered. Figure 3 demonstrates the smooth transition of the boiling curve $q_F(T_F, P)$ from the linear state ($P = 0$) to the final nonlinear state ($P = 1$) in Figure 2*b*.

The discrete nonlinear problem (25) with the P-dependent heat transfer condition (32) can be represented as

$$\boldsymbol{\mathcal{G}}(\boldsymbol{t}, P) := \big(\boldsymbol{K} + \boldsymbol{M}_P(\boldsymbol{t})\big)\boldsymbol{t} - \boldsymbol{g} = 0. \tag{33}$$

Note that $\boldsymbol{M}_P(\boldsymbol{t})$ depends on P via $\boldsymbol{M}_P(\boldsymbol{t}) = \mathrm{diag}\big(\alpha_P(T_j)\big)_{0\le j\le N}$ with $\alpha_P(T_F) = \frac{\Pi_2}{\Lambda}\frac{q_F(T_F,P)}{T_F}$ and $q_F(T_F, P)$ as in (32). For each $P \in [0, 1]$ the set of *homogeneous* solutions (i.e. $\boldsymbol{t}$ =constant) of this system can be easily computed. Starting on a branch of homogeneous solutions we apply a continuation algorithm[2] to $P \to \boldsymbol{\mathcal{G}}(\boldsymbol{t}, P) = 0$ and determine bifurcations points on the homogeneous branches from which branches of heterogeneous solutions originate. These strategies and the resulting bifurcation diagrams are discussed in the following.

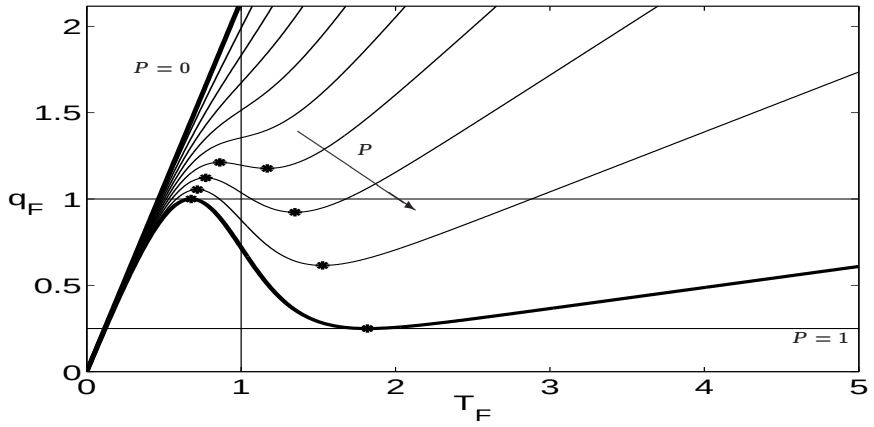

Figure 3: *Controlling the degree of nonlinearity of the boiling curve via the nonlinearity parameter P. Shown is the smooth transition from a linear profile ($P = 0$) towards the physical boiling curve (heavy; $P = 1$) with increasing P (arrow). The stars denote the local maxima and minima that occur for P beyond some non-zero lower limit.*

5 Numerical experiments: a case study

In this section we consider the discrete steady-state problem for a fixed parameter set, namely for $\Lambda = 0.2$, $D = 0.2$, $\Pi_1 = 4$, $\Pi_2 = 2$ and $W = 1$. The set of steady-state solutions is determined with the method explained in Section 4. Homogeneous solutions are obtained by means of a standard Newton-type root-finding algorithm applied to (13); heterogeneous solutions follow from continuation of the nonlinear system (33) in the nonlinearity parameter P. Note that for smooth boiling curves (i.e. $W > 0$) the truncated Fourier expansion on which our discretization method is based exhibits exponential convergence and thus already for modest values of N the discrete problem (25) is a highly accurate approximation of the continuous solution. In our experiments we use $N = 128$.

5.1 Homogeneous solutions

The homogeneous steady-state solutions (14) are uniquely determined by the constant interface temperature T_F as in (13). This interface temperature is given by the (multiple) intersection(s) of the boiling curve with the normalised heat supply $q_H^* = \Pi_2^{-1}$ (see Figure 2*b*). For the determination of the physically-meaningful homogeneous solutions it is sufficient to

[2]Here an in-house algorithm has been used, which is based upon techniques described in Govaerts (2000). Elaboration on this continuation algorithm is beyond the present scope.

solve (13) for $P = 1$. However, to obtain bifurcation points from which branches of heterogeneous solutions originate we have to determine the homogeneous branches in the entire range $0 \leq P \leq 1$. These branches readily follow from solving (13) in this P-range. Two essentially different situations can be distinguished, as illustrated in Figure 4, namely: (i) one solution $T_F^{(1)}$ for $0 \leq P < P_B$ (Figure 4*a*); (ii) three solutions $(T_F^{(1)}, T_F^{(2)}, T_F^{(3)})$ for $P_B < P \leq 1$ (Figure 4*c*). Both situations are connected through the degenerate case $P = P_B$, for which the local minimum of the boiling curve $q_F(\cdot, P_B)$ touches the normalised heat supply Π_2^{-1}, causing the second and third solutions to coincide (Figure 4*b*). Thus the system undergoes a qualitative change at $P = P_B$ through a so-called tangent bifurcation (see Ott (2002)).

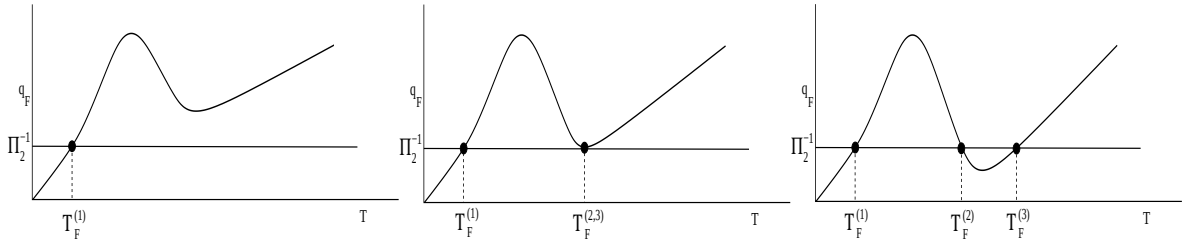

a) $0 \leq P < P_B$ *b)* $P = P_B$ *c)* $P_B < P \leq 1$

Figure 4: *Homogeneous solutions to the nonlinear system as a function of the nonlinearity parameter P. Transition from the single-solution state (panel a) to the triple-solution state (panel c).*

A diagram of the solutions as a function of the nonlinearity parameter P is shown in the bifurcation diagram in Figure 5, where solutions are represented in terms of the functional $T_\Sigma = \sum_n \widetilde{T}_n$. The heavy curves are the solution branches corresponding to the homogeneous solutions (14). The lower (nearly-horizontal) branch coincides with the intersection $T_F^{(1)}$ that exists for all $0 \leq P \leq 1$; the upper branch, with a turning point at P_B, coincides with the two intersections $T_F^{(2,3)}$ that exist only in the interval $P_B \leq P \leq 1$ (here $P_B \approx 0.926$). The lower and upper legs of this upper branch, connected at the turning point, correspond to $T_F^{(2)}$ and $T_F^{(3)}$, respectively. The solid curves are heterogeneous solution branches that originate from pitchfork bifurcations (dots) on the $T_F^{(2)}$-branch. An analysis of these bifurcation points is presented in the next section.

5.2 Bifurcation points on branches of homogeneous solutions

Starting on the branches of homogeneous solutions we found the bifurcation diagram shown in Figure 5.
Bifurcations can only occur at P-values for which the Jacobian of $\boldsymbol{\mathcal{G}}$ with respect to $\boldsymbol{t}$ is singular (see e.g. Govaerts (2000)). This Jacobian is given by

$$\boldsymbol{J} = \frac{\partial \boldsymbol{\mathcal{G}}}{\partial \boldsymbol{t}} = \boldsymbol{K} + \boldsymbol{Q}(\boldsymbol{t}), \qquad \boldsymbol{Q}(\boldsymbol{t}) = \operatorname{diag}\big(\gamma(T_k)\big)_{0 \leq k \leq N}, \qquad \gamma(T) := \frac{\Pi_2 \dot{q}_F(T)}{\Lambda}. \tag{34}$$

On a homogeneous branch we have $\boldsymbol{t} = T_F(1, \ldots, 1)^T$ and thus $\boldsymbol{Q}(\boldsymbol{t}) = \gamma(T_F)\boldsymbol{I}$, with $\boldsymbol{I}$ the identity matrix and T_F the homogeneous interface temperature. Hence we obtain

$$\boldsymbol{J} = \boldsymbol{K} + \gamma(T_F)\boldsymbol{I} = \boldsymbol{V}\boldsymbol{K}_S\boldsymbol{V}^{-1} + \gamma(T_F)\boldsymbol{I} = \boldsymbol{V}\boldsymbol{J}_S\boldsymbol{V}^{-1}, \tag{35}$$

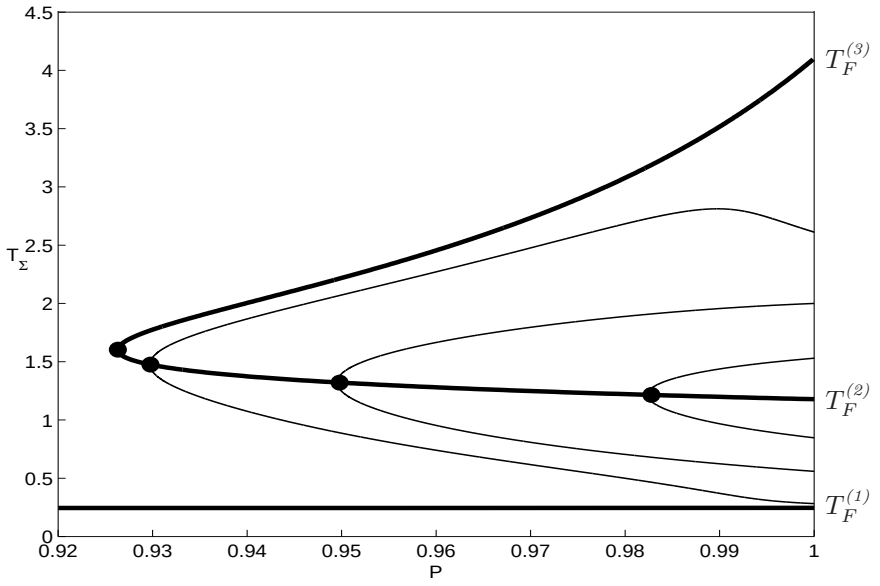

Figure 5: *Bifurcation diagram for the nonlinearity parameter P and fixed system parameters $\Lambda = 0.2$, $D = 0.2$, $\Pi_1 = 4$, $\Pi_2 = 2$ and $W = 1$. Heavy curves correspond to homogeneous solutions; solid curves correspond to heterogeneous solutions. Filled circles represent bifurcations. The left-most bifurcation is the tangent bifurcation that leads to multiple homogeneous solutions; the bifurcations from which the heterogeneous branches emerge are pitchfork bifurcations.*

with $\boldsymbol{J}_S = \mathrm{diag}\big(n\pi \tanh(n\pi D) + \gamma(T_F)\big)_{0\le n\le N}$. Thus on the homogeneous branches we have an explicit eigenvector decomposition of the Jacobian. The eigenvalues and corresponding eigenvectors are given by

$$\begin{aligned} \lambda_n &= n\pi \tanh(n\pi D) + \gamma(T_F) \\ \boldsymbol{v}_n &= (\cos(n\pi x_0), \ldots, \cos(n\pi x_N))^T, \quad 0 \le n \le N. \end{aligned} \tag{36}$$

The eigenvector $\boldsymbol{v}_n$ coincides with the n-th Fourier mode. The Jacobian is singular if one or more of its eigenvalues λ_n vanish. Because $n\pi \tanh(n\pi D) \ge 0$ for all $n \ge 0$, this can only happen if $\gamma(T_F) \le 0$. Thus a bifurcation on a homogeneous solution branch can only occur for those T_F for which the boiling curve has a negative slope ($\dot{q}_F \le 0$). From Figure 4 it follows that only intersection $T_F^{(2)}$ satisfies this criterion. This explains why bifurcations are restricted to the $T_F^{(2)}$-branch in the bifurcation diagram (Figure 5). This implies that bifurcations – and thus multiple (heterogeneous) solutions – can only occur for surface temperature values in the transition range of the boiling curve. Figure 6 displays γ (heavy curve) as a function of P on the $T_F^{(2)}$-branch together with $F(n) = -n\pi \tanh(n\pi D)$ (dashed lines) for various n.
The intersections $\gamma = F(n)$ correspond to $\lambda_n = 0$. These eigenvalues are simple and the corresponding eigenspace is one-dimensional. From basis results in analysis (eg., Thm. 28.3 in Deimling (1985)) it follows that at these P-values the system undergoes a bifurcation. These four P-values correspond to the positions of the bifurcations (filled circles) on the $T_F^{(2)}$-branch (Figure 5). From Figure 6 we see that for the case considered in this section the system has $\lambda_n = 0$ only for $n = 0, 1, 2, 3$. The bifurcations on the $T_F^{(2)}$-branch in Figure 5 correspond from left to right to the cases $n = 0$, $n = 1$, $n = 2$ and $n = 3$. This ordering

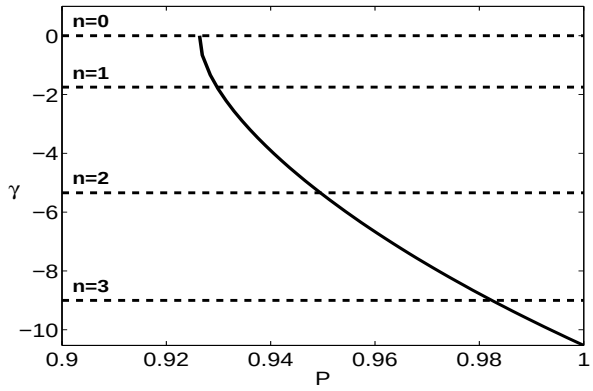

Figure 6: *Function* $P \rightarrow \gamma(T_F(P)) = \Pi_2 \dot{q}_F(T_F(P))/\Lambda$ *along the homogeneous* $T_F^{(2)}$*-branch (heavy). The dashed horizontal lines are the values of* $F(n) = -n\pi \tanh(n\pi D)$ *for* $n = 0, 1, 2, 3$*. Intersections of* γ *with* $F(n)$ *correspond to a singular Jacobian* $\boldsymbol{J}$ *and thus to a bifurcation.*

results from the monotonic dependence of γ on P. It also follows that in the range $P \in [0, 1]$ bifurcation points on the homogeneous $T_F^{(2)}$-branch with constant temperature values $T_{F,P}$ occur for those wave numbers $n = 0, 1, 2, \ldots$ that satisfy the inequality

$$n\pi \tanh(n\pi D) + \gamma(T_{F,1}) \leq 0. \tag{37}$$

5.3 Heterogeneous solutions

The eigenvector $\boldsymbol{v}_n$ corresponding to an eigenvalue λ_n is given in (36). Hence, it follows that for $n \geq 1$ a *heterogeneous discrete* solution of the form

$$T_F(\boldsymbol{x_j}) = T_F^{(2)} + \epsilon \cos(n\pi x_j), \quad 0 \leq j \leq N, \ \epsilon \downarrow 0, \tag{38}$$

emerges from the bifurcation point corresponding to λ_n (Thm. 28.3 in Deimling (1985)). Due to the symmetry property derived in Section 4.1 we can conclude that there exists a pair of heterogeneous solutions

$$T_F \quad \text{as in (38)}, \quad T_F^*(x) = T_F(x + \frac{1}{n}). \tag{39}$$

(Where T_F^* is a discrete solution in the sense as explained in Theorem 4). The first bifurcation ($n = 0$; turning point on the $T_F^{(2)}$-branch) corresponds with a superimposed zero-th Fourier-mode $\boldsymbol{v}_0$, hence the solution that emerges from this bifurcation point is homogeneous. Thus the first bifurcation point ($n = 0$) is of tangent type (shown schematically in Figure 4*b*) resulting in two homogeneous solutions. The bifurcations for $n > 0$ involve non-coinciding superimposed modes that, due to symmetry properties (Theorems 2 and 4), form conjugate pairs of heterogeneous solutions; hence for $n > 0$ we have pitchfork bifurcations.

The bifurcation diagram in Figure 5 shows the structure of the solution branches as a function of the continuation parameter P. Figure 7*a* shows the evolution of the heterogeneous solutions near the first pitchfork bifurcation ($n = 1$; $P = 0.9297$) for several P-values slightly larger than $P = 0.9297$.

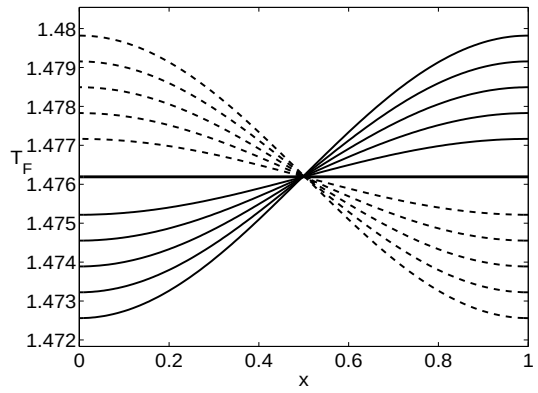

a) First pitchfork bifurcation ($P = 0.9297$).

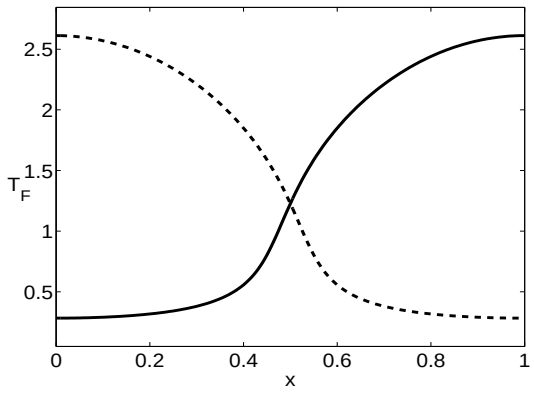

b) Corresponding final state ($P = 1$).

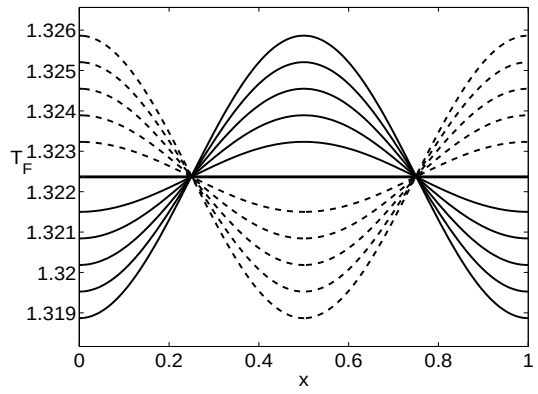

c) Second pitchfork bifurcation ($P = 0.9495$).

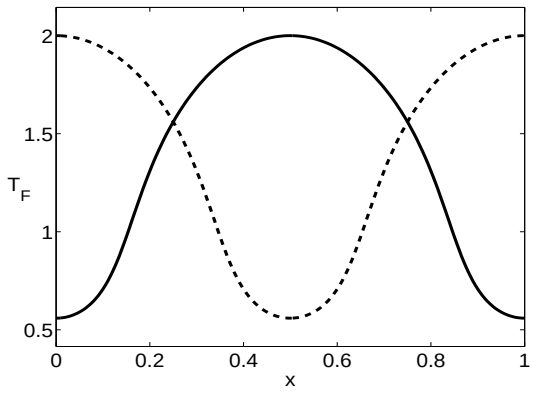

d) Corresponding final state ($P = 1$).

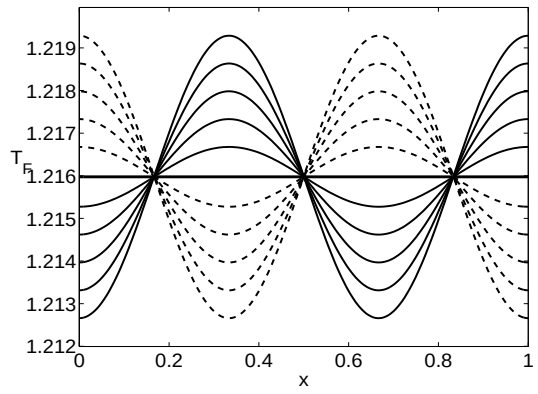

e) Third pitchfork bifurcation ($P = 0.9824$).

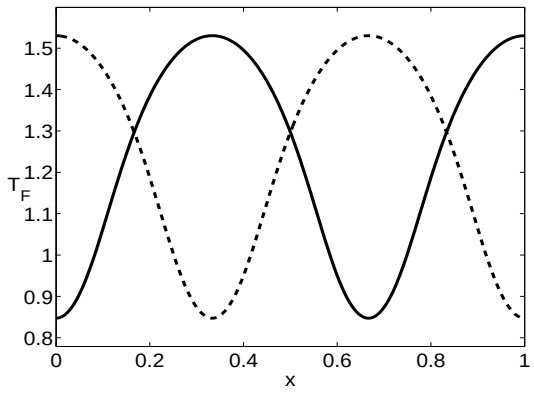

f) Corresponding final state ($P = 1$).

Figure 7: *Heterogeneous solutions originating from pitchfork bifurcations (left column) and corresponding final states at $P = 1$ (right column). The heavy line in panel a represents the bifurcating homogeneous solution; solid and dashed curves represent the corresponding conjugate pair of heterogeneous solutions. The final states are steady-state solutions of* (25).

The final (i.e. physically-meaningful) heterogeneous states at $P = 1$ are shown in Figure 7*b*. At this pitchfork bifurcation the heterogeneous solutions originate from the first non-constant Fourier mode (i.e. $n = 1$ in (39)), which can be clearly seen in Figure 7*a*. Figure 7*b* shows that the form of this first Fourier mode is roughly maintained throughout the evolution from the pitchfork bifurcation to the final state at $P = 1$. For the second ($n = 2$) and third ($n = 3$) bifurcations similar behaviour occurs. In Figure 7*c* ($n = 2$) and Figure 7*e* ($n = 3$) it is shown how heterogeneous solutions originate from these bifurcations. The final states ($P = 1$) are given in Figure 7*d* and Figure 7*f*, respectively. The final states at $P = 1$ (right column of Figure 7) are the physically-meaningful heterogeneous steady-state solutions at the heater-fluid interface Γ_F. These solutions are denoted *mode-n solutions* (with $n \in \{1, 2, 3\}$). Figure 8 shows the temperature distributions in the heater corresponding to these mode-n solutions, revealing that the heterogeneous features occur mainly in lateral (i.e. x-wise) direction.

One further interesting feature that can be observed in Figure 7 is the following. The mode-n ($n \in \{1, 2, 3\}$) solution T_F emerges from a perturbation $\boldsymbol{v}_n \in V_n$. In a neighbourhood of the bifurcation point we have a heterogeneous solution $T_F \in V_n$ and thus, due to Theorem 4, also a dual solution T_F^* with the symmetry property $T_F^*(x) = T_F(x + \frac{1}{n})$. It turns out that during the continuation from the bifurcation point to the final value $P = 1$ the heterogeneous solution T_F *remains in* V_n and thus the symmetry property $T_F^*(x) = T_F(x + \frac{1}{n})$ holds for the whole range $P \in [P_{\text{bifur}}, 1]$.

Remark 4 An explanation for this "conservation of symmetry" property (for $P \in [P_{\text{bifur}}, 1]$) is the following. From Theorem 3 and Remark 3 it follows that the operator $\boldsymbol{\mathcal{G}}(\boldsymbol{t}, P)$ has the property $\boldsymbol{\mathcal{G}}(\cdot, P) : V_k^N \to V_k^N$ for all $P \in [0, 1]$ and all $k \geq 1$ such that $N \bmod k = 0$. Note that a homogeneous solution lies in V_k^N for all k. Let $P = P_n$ be such that $\lambda_n = 0$ ($n \geq 1$) holds, i.e. P_n corresponds to a mode-n bifurcation point. We take N such that $N \bmod n = 0$ is satisfied. In a neighbourhood of P_n we can consider

$$\boldsymbol{\mathcal{G}}(\cdot, P) : V_n^N \to V_n^N. \tag{40}$$

Starting from the bifurcation point we then have for increasing P a heterogeneous solution, starting from $T_F^{(2)} + \epsilon \boldsymbol{v}_n \in V_n^N$ (with $\epsilon = P - P_n$), which due to (40) *remains in* V_n^N, until a new singularity is encountered. Thus during the continuation the solution $T_F = T_{F,P}$ remains in V_n^N and has a dual solution with the symmetry property $T_F^*(x) = T_F(x + \frac{1}{n})$ (cf. Theorem 4).

First results of a stability analysis show that all heterogeneous solutions as well as the homogeneous solution $T_F^{(2)}$ are unstable as a function of time. Only the homogeneous solutions in the nucleate ($T_F^{(1)}$) and film ($T_F^{(3)}$) boiling regimes are stable. If we use a slightly perturbed heterogeneous mode-n stationary solution as initial condition for the parabolic nonlinear problem (4) then the solution of this instationary problem converges to one of the two homogeneous solutions $T_F^{(1)}$ or $T_F^{(3)}$. The time scale for which the mode-n heterogenity is still clearly visible in the instationary solution is significant for small n-values and decreases rapidly for larger n-values.

6 Numerical experiments: variation of system parameters

The steady-state pool boiling model is determined by the system parameters (Λ,D,Π_1,Π_2,W), cf. Section 2.2. These parameters control the following physical phenomena: (i) fluid-heater

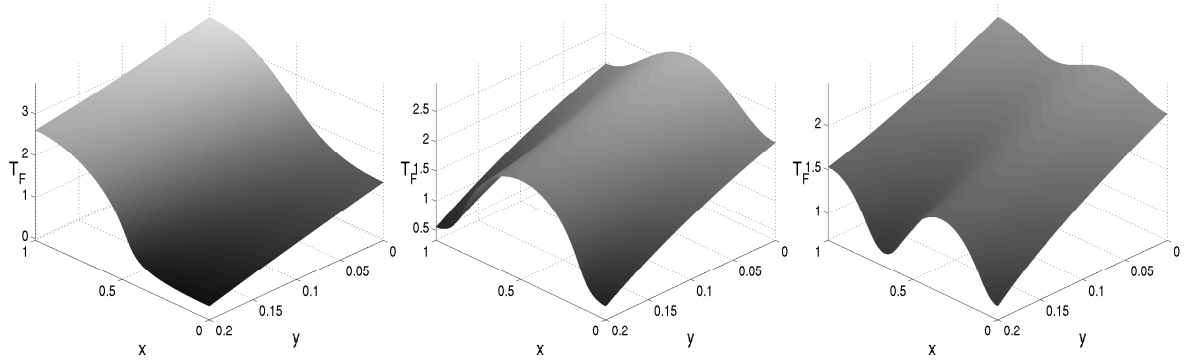

a) Mode-1 solution. *b) Mode-2 solution.* *c) Mode-3 solution.*

Figure 8: *Temperature distributions $T(x, y)$ for the mode-n solutions. Heat supply and heat extraction is through the lines $y = 0$ and $y = 0.2$, respectively.*

interaction via the boiling curve (Π_1 and W); (ii) properties of the heater (Λ and D); (iii) heating conditions (Π_2). Changes in the steady-state behaviour due to variation of these parameters is investigated below. We first perform a bifurcation analysis for the system parameters similar to that for the continuation parameter P (Section 6.1). Then we study the physical changes in steady-state solutions with changing parameter values (Section 6.2). The bifurcation analysis is carried out with the continuation procedure proposed in Section 4, using the steady-state solutions determined in Section 5 as initial conditions.

6.1 Bifurcation analysis for the system parameters

Regions of existence of bifurcations and multiple solutions
Bifurcations imply multiple solutions and occur (only) if the $T_F^{(2)}$-branch exists (see Section 5), or equivalently, if the boiling curve and the normalised heat supply $q_H^* = \Pi_2^{-1}$ have three intersections. This is equivalent to the condition $1 \leq \Pi_2 \leq \Pi_1$. Furthermore, it follows from (37) that within this regime mode-n solutions ($n \geq 1$) exist only if the inequality (37) is satisfied. The homogeneous solution $T_{F,1}$ on the $T_F^{(2)}$-branch depends on the parameters Π_1, Π_2, W, thus we write $T_{F,1} = T_{F,1}(\Pi_1, \Pi_2, W)$. Using the definition of γ in (34) we obtain the condition

$$\Lambda \leq -\frac{\Pi_2 \, \dot{q}_F \left(T_{F,1}(\Pi_1, \Pi_2, W)\right)}{n\pi \tanh(n\pi D)} \tag{41}$$

from (37) for the existence of a mode-n solution ($n \geq 1$). We introduce the notation

$$\Lambda^{(n)}(\Pi_1, \Pi_2, D, W) := -\frac{\Pi_2 \, \dot{q}_F \left(T_{F,1}(\Pi_1, \Pi_2, W)\right)}{n\pi \tanh(n\pi D)}.$$

This function bounds the region of existence of mode-n solutions ($\Lambda \leq \Lambda^{(n)}(\Pi_1, \Pi_2, D, W)$) and is therefore a separatrix. Due to $\dot{q}_F(T_F^{(2)}) < 0$ we have $\Lambda^{(n)} > 0$. As a function of n the separatrices are strictly ordered: $\Lambda^{(1)} > \Lambda^{(2)} > \cdots > \Lambda^{(\infty)}$. This implies that (i) regions of existence of mode-n solutions are smaller with increasing wave number n and (ii) within the

range $1 \leq \Pi_2 \leq \Pi_1$ heterogeneous solutions are restricted to the subregime $\Lambda > \Lambda^{(1)}$. We consider a given boiling curve with $W = 1$ and $\Pi_1 = 4$. Figure 9 shows $\Lambda^{(n)} = \Lambda^{(n)}(4, \Pi_2, D, 1)$ for $1 \leq n \leq 5$. The surfaces represent from left to right the separatrices $\Lambda^{(1)} > \Lambda^{(2)} > \ldots$; the region to the right of each separatrix is the region of existence of the corresponding mode-n solution. All $\Lambda^{(n)}$ vanish for $\Pi_2 = 1$ and $\Pi_2 = \Pi_1$, which is consistent with the fact that multiple solutions do not exist outside the range $1 \leq \Pi_2 \leq \Pi_1$.

In the hyperplanes $\Pi_2 = 1$ and $\Pi_2 = \Pi_1$ the system undergoes the tangent bifurcation that leads to the transition from one to three homogeneous solutions. On the separatrices $\Lambda^{(n)}$ the system undergoes pitchfork bifurcations that result in pairs of mode-n solutions. Thus for a given boiling curve these hyperplanes and separatrices represent bifurcations in the (Λ, Π_2, D)-parameter space. It should be noted that the qualitative behaviour is not dramatically changed if the thickness of the heater (D) is changed. The regions do only quantitatively change with D.

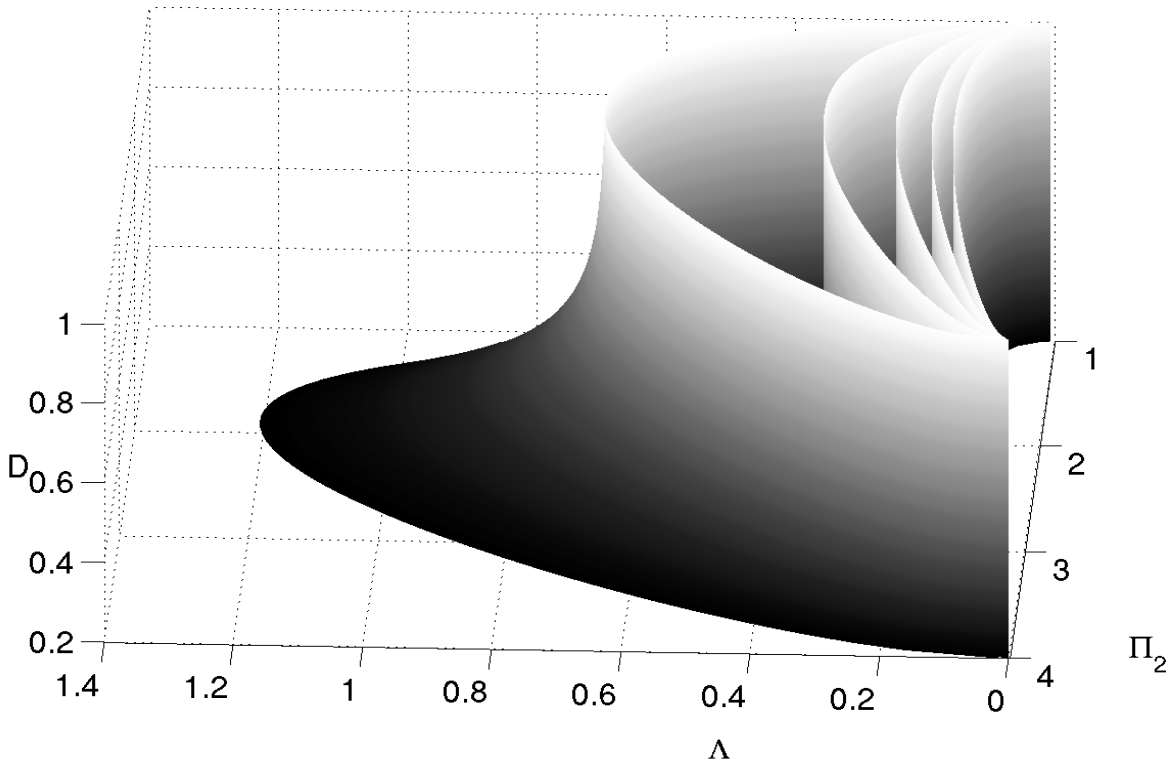

Figure 9: *Separatrices $\Lambda^{(n)}$ for $1 \leq n \leq 5$ in case of a given boiling curve ($W = 1$; $\Pi_1 = 4$). The surfaces coincide from left to right with separatrices $\Lambda^{(1)} > \Lambda^{(2)} > \ldots$; the region to the right of each separatrix is the region of existence of the corresponding mode-n solution.*

Effect of changes in the boiling curve: variation of W and Π_1

For an arbitrary transition width W homogeneous steady-state solutions T_F are given as solution of $q_F(T_F) = \Pi_2^{-1}$. From the shape of the boiling curve q_F it is clear that variation of W does not result in qualitative changes in the set of homogeneous solutions. We illustrate

this in Figure 10*a* for the boiling curves with $W = 1$ (heavy), $W = 0.1$, $W = 0.5$ (solid) and corresponding homogeneous solutions $T_F^{(1,2)}$ (dots) for $\Pi_2 = 2$. (Note that the third intersection $T_F^{(3)}$ is not shown.) Heterogeneous mode-n solutions originate from bifurcations on the $T_F^{(2)}$-branch occurring when $F(n) = \gamma(T_F^{(2)})$ holds (see Section 5.2). Figure 10*b* shows $F(n)$ and $\gamma(T_F^{(2)})$ for $0.5 \leq W \leq 1$ and $n \geq 1$. The boiling curve becomes steeper for smaller W-values, resulting in decreasing γ-values. This causes the number of intersections (and thus bifurcations) to increase monotonically with decreasing W. Narrowing the transition region thus progressively augments the number of mode-n solutions and increases the wave-number range $1 \leq n \leq n_{max}$ for which heterogeneous solutions exist. For $W = 1$ three intersections occur and thus we have $n_{max} = 3$; for $W = 0.5$ and $W = 0.1$ the wave-number ranges increase to $n_{max} = 5$ and $n_{max} = 21$, respectively.

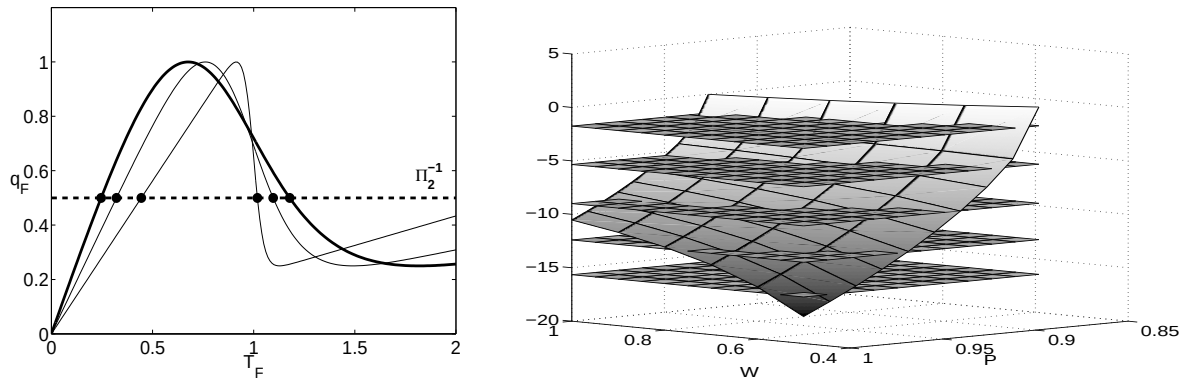

a) $q_F(T_F)$ for $W \in \{0, 0.5, 0.1\}$. *b) Intersections $F(n) \cap \gamma(T_F)$.*

Figure 10: *Effect of changing transition width W. Panel a illustrates the qualitative invariance of the solutions of $q_F(T) = \Pi_2^{-1}$ (dots) w.r.t. variation in W. The heavy curve is the boiling curve for the case $W = 1$. The other curves are for $W = 0.5$ and $W = 0.1$. Panel b shows $F(n)$ for $n > 0$ (parallel planes) and γ (surface) as a function of P and W. The number of intersections $F(n) \cap \gamma$ (implying mode-n solutions) grows with decreasing W.*

Figure 11*a* shows the bifurcation diagram corresponding to the continuation parameter P for the case $W = 0.5$. (Compare with the case $W = 1$ in Figure 5.) Figure 11*b* shows the $T_F^{(2)}$-branches and corresponding pitchfork bifurcation points (dots) for the transition widths $W = (0.1, 0.2, 0.5, 1)$.

The heat flux ratio Π_1 influences the boiling curve in a manner comparable to the continuation parameter P and changes thus have similar effects. This is demonstrated in Figure 12*a* for the case of a physical boiling curve ($P = 1$) with transition width $W = 1$. Homogeneous solutions correspond to intersections $q_F(T_F) = \Pi_2^{-1}$, which occur according to the scenario sketched for increasing P in Figure 4. Increasing Π_1 lowers the local minimum (Leidenfrost point) and consequently causes a transition from one ($\Pi_1 < \Pi_2$) to three ($\Pi_1 > \Pi_2$) solutions via the tangent bifurcation at $\Pi_1 = \Pi_2$. On the $T_F^{(2)}$-branch a pitchfork bifurcation occurs if $F(n) = \gamma(T_F^{(2)})$ holds. In Figure 12*b* the graphs of $F(n)$ and $\gamma(T_F^{(2)})$ as a function of Π_1 and W are given. Note the similarity between Figure 12*b* and Figure 10*b*. It follows that $\gamma(T_F^{(2)})$ decreases monotonically with increasing Π_1. Hence, the number of intersections $F(n) = \gamma(T_F^{(2)})$ (and thus of mode-n solutions) increases with increasing Π_1. The bifurcation diagram for Π_1 is qualitatively similar to that for P (Figure 5). Furthermore, increasing Π_1

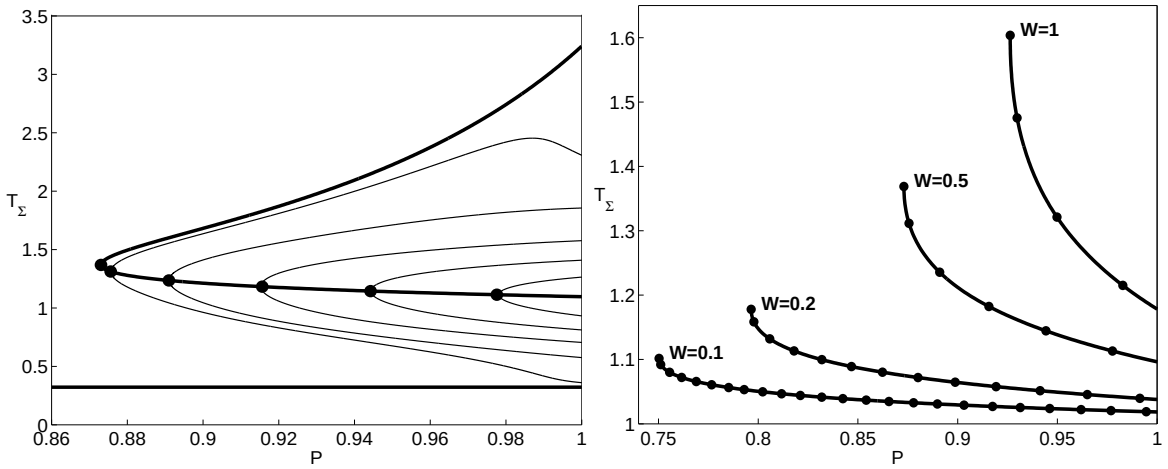

a) Bifurcation diagram for $W = 0.5$. *b) $T_F^{(2)}$-branch for several W values.*

Figure 11: *Set of mode-n solutions for decreasing transition width W. Panel a shows the bifurcation diagram for $W = 0.5$. Panel b shows the $T_F^{(2)}$-branches and corresponding pitchfork bifurcations (dots) for the indicated transition widths W.*

has a effect similar to decreasing the transition width W: The wave-number range in which bifurcations exist is enlarged.

The above reveals that variations of W and Π_1 (in realistic ranges) do not lead to qualitative changes in the behaviour of the system. Therefore it is no severe restriction to consider only one fixed boiling curve. In the remainder we use as default the boiling-curve parameters $\Pi_1 = 4$ and $W = 1$ and investigate the role of the heating conditions (Π_2) and heater properties (Λ and D) on the behaviour of the pool boiling model.

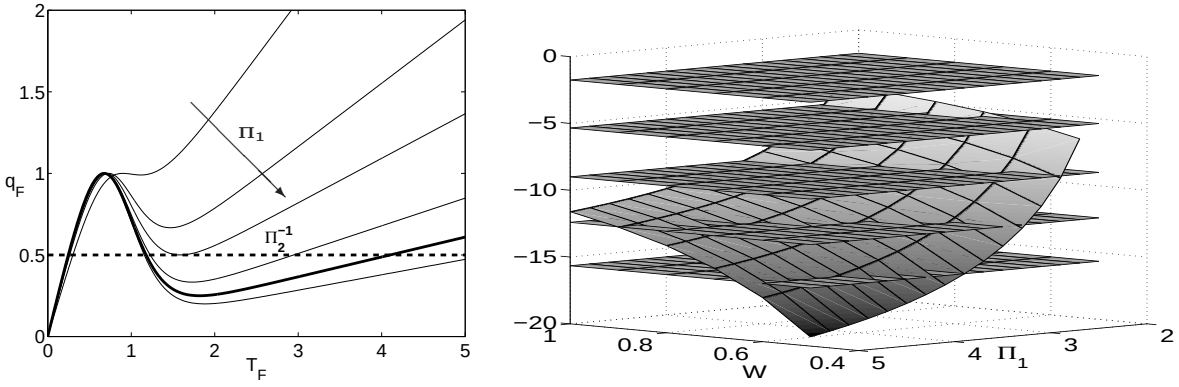

a) Boiling curve for several Π_1 values. *b) Intersections $F(n) \cap \gamma(T_F)$.*

Figure 12: *Effect of changing heat ratio Π_1 on the steady-state behaviour. Panel a shows the boiling curve as a function of Π_1 (cf. Figure 3). The heavy curve is the boiling curve for $W = 1$. Panel b shows $F(n)$ for $n > 0$ (parallel planes) and γ as a function of W and Π_1. The number of intersections $F(n) \cap \gamma$ (implying mode-n solutions) grows with increasing Π_1.*

Effect of changes in the heating conditions: variation of Π_2

The heating conditions (Π_2) determine the regions of existence of multiple solutions (see before) and thus the global boiling mode. Multiple (heterogeneous) solutions are restricted to the regime $1 \leq \Pi_2 \leq \Pi_1$. Outside the range $1 \leq \Pi_2 \leq \Pi_1$ only one homogeneous solution – and consequently only one homogeneous boiling state – exists, namely $T_F^{(1)}$ (nucleate boiling) for $\Pi_2 > \Pi_1$ and $T_F^{(3)}$ (film boiling) for $0 \leq \Pi_2 < 1$. The link between multiplicity of steady-state solutions and heating conditions is consistent with laboratory experiments (see Auracher & Marquardt (2004)) and is a fundamental property of pool boiling systems.

Figure 14*a* shows a typical bifurcation diagram for Π_2 with heater properties $\Lambda = 0.2$ and $D = 0.2$. The homogeneous branches are combined into the heavy curve and connected via the turning points at $\Pi_2 = 1$ and $\Pi_2 = \Pi_1 (= 4)$. These turning points correspond to the boundaries of the parameter range $1 \leq \Pi_2 \leq \Pi_1$ and are the tangent bifurcations that lead to multiple homogeneous solutions. The lower and upper sections of the combined homogeneous branch coincide with the $T_F^{(1)}$-and $T_F^{(3)}$-branches, respectively. The centre section corresponds to the $T_F^{(2)}$-branch. The heterogeneous branches corresponding to the mode-n solutions (solid) originate pair-wise from this branch and form closed concentric loops, with n increasing from $n = 1$ in inward direction (here $n = 1, 2, 3$). The dashed line refers to the case study of Section 5.

The fact that the heterogeneous branches are closed curves can be explained as follows. Introduce the function

$$g : \Pi_2 \to \Pi_2 \, \dot{q}_F(T_F(\Pi_2)), \quad \Pi_2 \in [1, 4],$$

with $T_F(\Pi_2)$ such that $q_F(T_F) = \Pi_2^{-1}$ and $\dot{q}_F(T_F) \leq 0$. From the graph of q_F (for the case $\Pi_1 = 4,\ W = 1$) it follows that $g(1) = g(4) = 0$, $g(x) \leq 0$ for all $x \in [1, 4]$ and there is a unique $x^* \in (0, 4)$ where g attains its minimal value, cf. Figure 13.

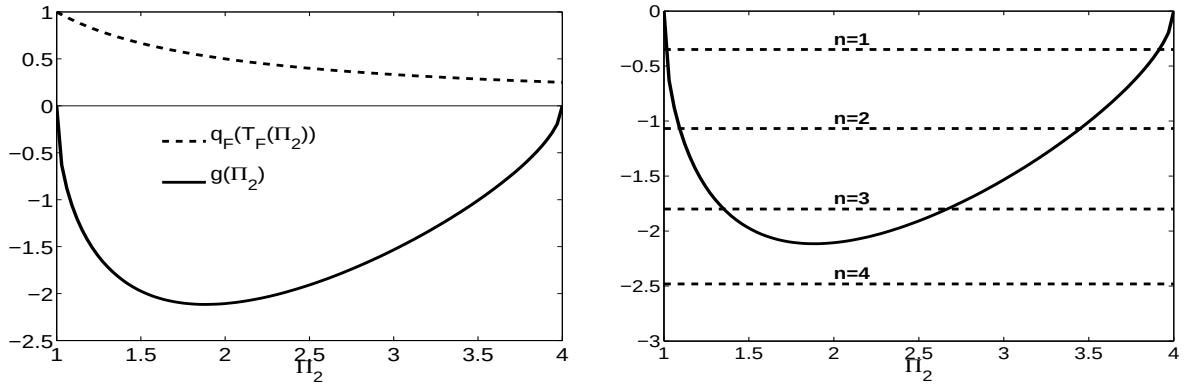

a) Profile of q_F and g on the $T_F^{(2)}$-branch. *b) Insections of g and $-\Lambda n\pi \tanh(n\pi D)$, cf. (42).*

Figure 13: *Effect of changing heating condition (Π_2) on the steady-state behaviour. Panel a shows the profiles of q_F (dashed) and $g = \Pi_2 \dot{q}_F$ (heavy) on the $T_F^{(2)}$-branch. Panel b shows g (heavy) and $-\Lambda n\pi \tanh(n\pi D)$ for $n \geq 1$ (dashed) on the $T_F^{(2)}$-branch. The intersections between g and dashed lines occur pair-wise and correspond with one mode-n solution branch.*

Bifurcations on the homogeneous $T_F^{(2)}$-branch occur if an eigenvalue of the Jacobian equals zero, i.e., cf. (36), if $T_F = T_F(\Pi_2)$ is such that

$$\Pi_2 \, \dot{q}_F(T_F(\Pi_2)) = -\Lambda n\pi \tanh(n\pi D)$$

holds. The values for the parameters Λ and D are given ($\Lambda = D = 0.2$). Hence, a bifurcation occurs if $\Pi_2 \in [0, 4]$ and $n \geq 1$ are such that

$$g(\Pi_2) = -\Lambda n\pi \tanh(n\pi D). \tag{42}$$

From the shape of the graph of g it follows that solutions of (42) occur as pairs $\Pi_2^L(n)$, $\Pi_2^R(n)$ with $1 < \Pi_2^L(n) < \Pi_2^R(n) < 4$. Thus mode-$n$ bifurcation points occur in pairs, which leads to the closed heterogeneous branches in Figure 14*a*. Furthermore, the function $n \to \Pi_2^L(n)$ ($n \to \Pi_2^R(n)$) is strictly increasing (decreasing). This explains the specific ordering of the heterogeneous branches.

The bifurcation diagram (Figure 14*a*) provides information on the qualitative steady-state behaviour of the pool boiling system as a function of the heating conditions. Regimes $\Pi_2 > \Pi_1$ (nucleate boiling) and $0 \leq \Pi_2 < 1$ (film boiling) allow only one single solution branch. In the range $1 \leq \Pi_2 \leq \Pi_1$ (transition boiling) multiple solution branches occur. Multiplicity phenomena increase (more mode-n solutions) when Π_2 moves the borders of the interval $[1, \Pi_1]$ towards its centre. The multiple solution branches allow different steady states that the pool boiling system may have during transition from nucleate to film boiling (and *vice versa*) with changing heat supply.

Effect of changes in the heater properties: variation of Λ and D

We take a fixed value $\Pi_2 = 2$ and vary Λ and D. First we consider the effects of changing the non-dimensional thermal conductivity Λ, with a fixed $D = 0.2$. The resulting bifurcation diagram is shown in Figure 14*b*. The heavy lines are the homogeneous branches (which do not depend on Λ); the solid curves are the heterogeneous branches originating from the $T_F^{(2)}$-branch. The dashed line refers to the case study of Section 5. The wave number n of the mode-n solutions corresponding to the heterogeneous branches increases from $n = 1$ (rightmost heterogeneous branch) monotonically with decreasing Λ. This ordering can be explained as follows. A bifurcation point on the $T_F^{(2)}$-branch occurs if

$$\Lambda = -\frac{\Pi_2 \dot{q}_F(T_F)}{n\pi \tanh(n\pi D)} \tag{43}$$

holds, with T_F such that $q_F(T_F) = \Pi_2^{-1}$ and $\dot{q}_F(T_F) \leq 0$. This homogeneous solution T_F does not depend on Λ. Therefore, since D is also constant, for *every* $n \geq 1$ there is a unique solution $\Lambda(n)$ of (43). Furthermore, the function $n \to \Lambda(n)$ is strictly monotonically decreasing.

We now consider the effect of changes in the aspect ratio D, with a fixed $\Lambda = 0.2$. The corresponding bifurcation diagram is shown in Figure 14*c*. Heavy and solid lines again indicate homogeneous and heterogeneous branches; the dashed line refers to the case study of Section 5. This diagram resembles that for Λ in Figure 14*b* in that homogeneous branches do not depends on D and heterogeneous branches correspond from right to left with mode-n solutions with increasing wave number n. However, bifurcation points occur only for wave numbers $n \geq 4$. For the given Λ and Π_2 values the solutions corresponding to the wave numbers $1 \leq n \leq 3$ exist for any $D > 0$ and thus do not undergo bifurcations in this parameter range. This can be explained by similar arguments as used above for Λ. At a bifurcation point on the $T_F^{(2)}$-branch we now have

$$\tanh(n\pi D) = -\frac{\Pi_2 \dot{q}_F(T_F)}{n\pi\Lambda} \tag{44}$$

with T_F such that $q_F(T_F) = \Pi_2^{-1}$ and $\dot{q}_F(T_F) \leq 0$. This homogeneous solution T_F does not depend on D. For n too small ($1 \leq n \leq 3$) we have $-\frac{\Pi_2 \dot{q}_F(T_F)}{n\pi\Lambda} \geq 1$ and thus (44) does not have a solution. For n sufficiently large ($n \geq 4$) we have $0 < -\frac{\Pi_2 \dot{q}_F(T_F)}{n\pi\Lambda} < 1$ and thus (44) has a unique solution $D(n)$. One easily verifies that $n \to D(n)$ is strictly decreasing. For Λ sufficiently large we have $0 < -\frac{\Pi_2 \dot{q}_F(T_F)}{n\pi\Lambda} < 1$ for *all* $n \geq 1$ and then we have mode-n bifurcation points on the homogeneous $T_F^{(2)}$-branch for all $n \geq 1$.

From the above it readily follows that both with decreasing Λ and D the number of separatrices passed – and thus the number of bifurcation points occurring – increases. Since each new bifurcation implies a new pair of mode-n solutions, this implies that decreasing thermal conductivity (Λ) and/or relative heater thickness (D) induces more multiplicity and heterogeneity phenomena in our pool boiling model. Conversely, increasing thermal conductivity and/or relative heater thickness enhances homogeneity.

This effect of heater thickness is known from laboratory experiments (see e.g. Blum *et al.* (1996)). However, an essential difference between the effects of variation in Λ and in D is that increasing thermal conductivity at some point always causes vanishing of heterogeneous solutions, whereas for specific ranges of Λ (and Π_2) heterogeneous solutions are always present, irrespective of heater thickness. This can be seen from Figure 9. The bifurcation diagram in Figure 14*c* indicates that in this particular range of Λ and Π_2 bifurcations occur only for mode-n solutions with $n \geq 4$; solutions for $n = (1, 2, 3)$ exist for any aspect ratio D here.

6.2 Physical changes in steady-state solutions

Mode-n bifurcations occur in Λ- and D-directions if for a certain wave number n the eigenvalue λ_n of the Jacobian equals zero. Moving away from the bifurcation, by decreasing the system parameter, amplifies the heterogeneous features of the corresponding mode-n solutions in a similar way as demonstrated in Figure 7 for the continuation parameter P.

Figure 15*a* shows the change of the interface temperature $T_F(x)$ of the mode-1 solution with decreasing thermal conductivity Λ (solid curves) from its nearly homogeneous state at the bifurcation (heavy line; $\Lambda = 1.20$) to its state just above the lower bound $\Lambda = 0$ (heavy curve; $\Lambda = 0.05$). The plot reveals a progressive steepening of the profile with decreasing Λ to such an extent that it suggests a discontinuous profile for $\Lambda \downarrow 0$. This steepening results from the higher temperature gradients caused by the higher resistance to heat conduction due to lower thermal conductivity. For vanishing heat conduction this implies locally-infinite temperature gradients and consequently discontinuous profiles.

Figure 15*b* shows the change of $T_F(x)$ of the mode-4 solution (the lowest mode-n solution that originates from a bifurcation here) with decreasing aspect ratio D. The plot reveals that decreasing the relative heater thickness amplifies, similar to decreasing the thermal conductivity, the heterogeneous features of the mode-n. The progression suggests that, in contrast to the behaviour found for Λ, the solution now tends to a smooth profile for vanishing aspect ratio D. The heavy curve in Figure 15*b* corresponds to $D = 0.01$ and is believed to be a good approximation for the profile associated with the 'thin' heater ($D = 0$).

In Π_2-direction, mode-n bifurcations occur pair-wise and thus result in the essentially non-monotonic dependence of the solution on changing heating conditions. Figure 16 illustrates this behaviour for the profile $T_F(x)$ of the mode-2 solution by increasing Π_2 from $\Pi_2^L = \Pi_2^L(2)$ (left bifurcation point for $n = 2$) to $\Pi_2^R = \Pi_2^R(2)$ (right bifurcation point for $n = 2$). Thus the heterogeneous features of the profile are amplified (panel *a*) until at some $\Pi_2^L < \Pi_{2rev} < \Pi_2^R$

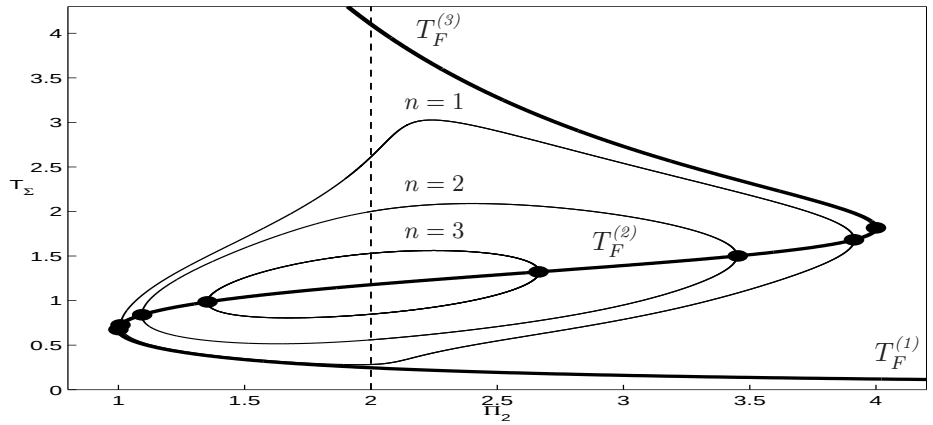

a) Bifurcation diagram for Π_2.

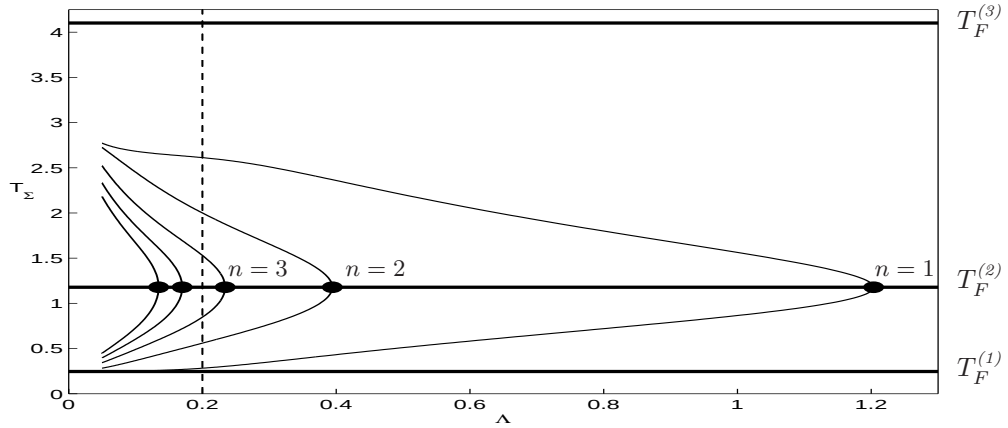

b) Bifurcation diagram for Λ.

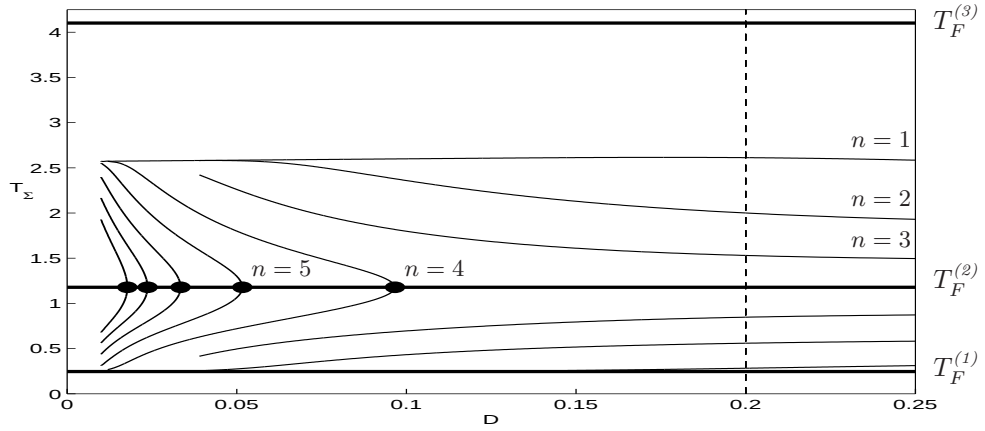

c) Bifurcation diagram for D.

Figure 14: *Bifurcation diagrams for system parameters* Π_2 *(*$\Lambda = 0.2$,$D = 0.2$*),* Λ *(*$\Pi_2 = 2$,$D = 0.2$*) and* D *(*$\Lambda = 0.2$, $\Pi_2 = 2$*). The intersections of the solution branches with the vertical dashed lines in the bifurcation diagrams for* Λ *and* Π_2 *coincide with the solutions at* $P = 1$ *in Figure 5.*

the process reverses (panel b; solid, heavy and dashed curves correspond to $\Pi_2 \leq \Pi_{2rev}$, $\Pi_2 = \Pi_{2rev}$ and $\Pi_2 > \Pi_{2rev}$, respectively) and the heterogeneous features diminish (panel c) and eventually vanish upon reaching Π_2^R. Note Π_{2rev} is defined as the Π_2-value for which the temperature difference $\Delta T_F = max(T_F) - min(T_F)$ reaches its maximum, in other words, the profile is the most heterogeneous.

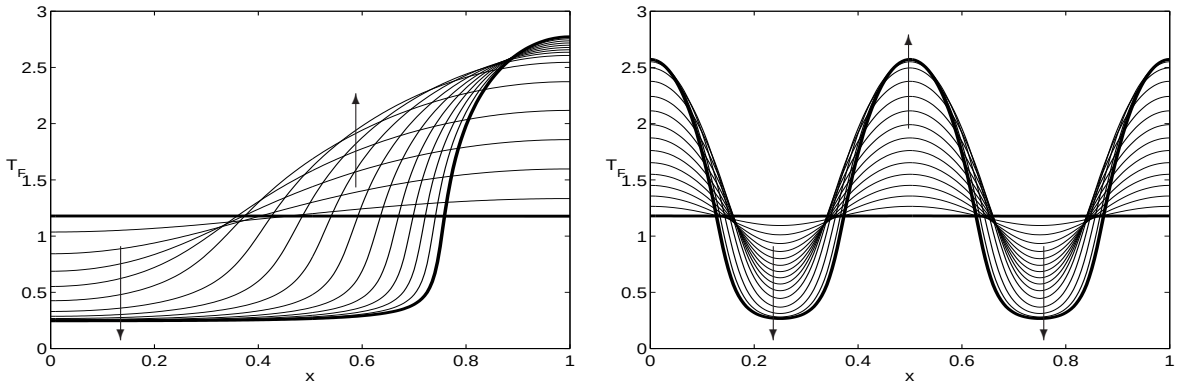

a) Mode-1 solution for Λ *b) Mode-4 solution for D*

Figure 15: *Changes in interface profile of indicated mode-n solutions as a function of Λ (panel a) and D (panel b). The heavy horizontal lines are the profiles at the bifurcation; the heavy curves are the profiles farthest away from the bifurcation. The solid curves are the intermediate states. The arrows indicate progression with* **decreasing** *system parameter Λ or D.*

7 Conclusions

In this paper we consider a two-dimensional heat equation with a nonlinear Neumann boundary condition on part of the boundary as a simple model for 2D pool boiling processes. The nonlinear Neumann boundary condition models the heat flux from the heater to the fluid by means of a nonlinear local heat flux temperature relation that is similar to the boiling curve. A key issue is the existence of multiple steady-state solutions with heterogeneous interface temperature. The seperation of variables technique leads to a reduction of the two-dimensional problem to a one-dimensional problem for the temperature at the heater-to-fluid interface, cf. (12). The latter problem is discretised using a collocation method. Both the continuous and discrete problem (at the interface) have a symmetry property (Theorems 2 and 4) that immediately implies multiplicity of heterogeneous solutions. These originate from bifurcations on a branch of homogeneous solutions. *The existence of symmetries (Theorem 2) and the conservation of symmetries (Theorem 1) are two fundamental properties of the model.* The multiple solution structure and its dependence on certain system parameters is studied through a bifurcation analysis applied to the discretised problem.

We outline a few main conclusions from the analysis.

There exist multiple (heterogeneous) steady-state solutions. Multiplicity and heterogeneity are restricted to those situations where transition boiling modes can occur; if only nucleate or film boiling regimes are possible, a unique solution exists, which is always homogeneous. Heterogeneous solutions represent temperature distributions that correspond to nucleate and

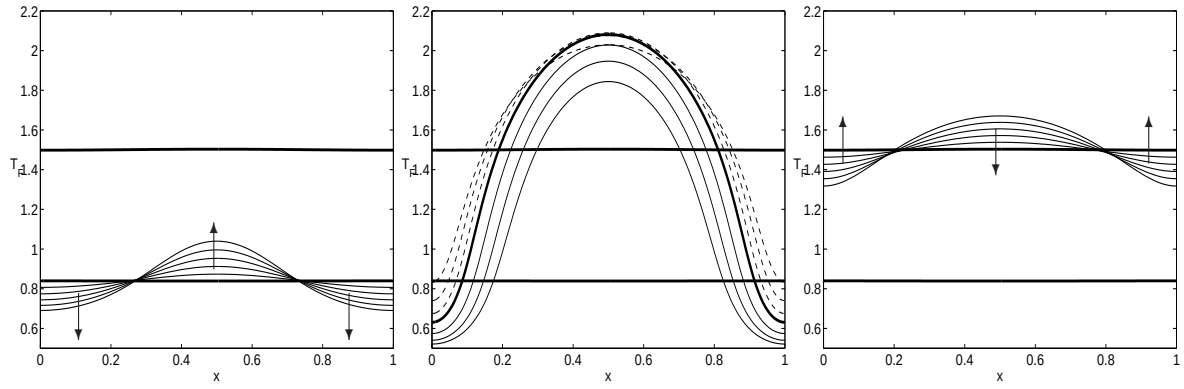

a) Near $\Pi_{2_{min}}$ *b) Near* $\Pi_{2_{rev}}$ *c) Near* $\Pi_{2_{max}}$

Figure 16: *Changes in interface profile of a mode-2 solution as a function of* Π_2*. The arrows indicate progression with* **increasing** *system parameter* Π_2*. The heavy horizontal lines are the profiles at the two corresponding bifurcations* $\Pi_{2_{min}}$ *and* $\Pi_{2_{max}}$*; the heavy curve in panel b is the most heterogeneous profile, which occurs at* $\Pi_{2_{rev}}$*. The arrows indicate progression of parameter* Π_2 *from* $\Pi_{2_{min}}$ *to* $\Pi_{2_{max}}$*.*

film boiling regions and thus are essentially two-mode boiling states. Heating conditions are modelled as a constant heat flux on the boundary opposite to the heater-fluid interface. Heat supply between critical heat flux (CHF) and Leidenfrost heat flux (LHF) implies three homogeneous solutions, each in one of the three boiling regimes. Heat supply outside this range results in only homogeneous solution, corresponding to either nucleate or film boiling. Heterogeneous solutions originate pairwise from pitchfork bifurcation points on the branch of homogeneous solutions in the transition regime of the boiling curve and can occur only under specific heating conditions. The actual steady-state solution attained at such pitchfork bifurcations is inherently unpredictable. Relevant system parameters are boiling curve coefficients (transition width W; CHF-LHF ratio Π_1) and heater properties (aspect ratio D; thermal conductivity Λ). Decreasing (one of) W, D and Λ and/or increasing Π_1 enlarges the set of heterogeneous solutions, suggesting this induces stronger multiplicity and heterogeneity of solutions of the pool boiling problem. However, variation of these parameters does not cause fundamental changes in the steady-state behaviour of the system. Multiplicity and heterogeneity only show a quantitative dependence on these parameters. The essential condition is $1 \leq \Pi_2 \leq \Pi_1$. If this condition is satisfied, there exists a homogeneous solution in the transition range of the boiling curve, leading to bifurcating pairs of heterogeneous solutions.

Important phenomena resulting from numerical simulations of our model are consistent with properties known from laboratory experiments. This suggests that the model provides an (at least qualitatively) adequate description of pool boiling.

Both the present model and the numerical techniques used can be extended relatively straightforward to 3D pool boiling systems. This is a topic of current research. Furthermore, results of a stability analysis of the steady-state solutions will be presented in a forthcoming paper. Preliminary results of this analysis reveal that steady-state solutions are always unstable, except for the two homogeneous solutions corresponding to the nucleate and film boiling regimes. Miscellaneous issues to be considered in future work may include the effect of different heating methods (see e.g. Darabi *et al.* (1999))) and stabilisation via active control

(see e.g. Auracher & Marquardt (2002)).

Acknowledgment

The presented work has benefitted greatly from the continuation algorithm kindly provided by Robert Grosch, Process Systems Engineering, RWTH Aachen.

References

Auracher, H. & Marquardt, W. 2002 Experimental studies of boiling mechanisms in all boiling regimes under steady-state and transient conditions. *Int. J. Therm. Sci.*, **41**, 586–598.

Auracher, H. & Marquardt, W. 2004 Heat transfer characteristics and mechanisms along entire boiling curves under steady-state and transient conditions. *J. Heat Fluid Flow*, **25**, 223–242.

Blum, J., Marquardt, W. & Auracher, H. 1996 Stability of Boiling Systems. *Int. J. Heat Mass Transfer*, **39**, 3021–3033.

Blum, J. & Marquardt, W. 1998 Objection to Haramura's criterions for temperature uniformity across the surface in transition boiling *Internal report LPT-1998-14, Lehrstuhl für Prozesstechnik, RWTH Aachen.*

Blum, J., Lüttich, T. & Marquardt, W. 1999 Temperature wave propagation as a route from nucleate to film boiling? In *Proceedings of the Second International Symposium on Two-Phase Flow Modelling and Experimentation, Rome, Vol 1* (ed. G.P. Celata, P. DiMarco & R.K. Shah), Edizioni ETS, Pisa.

Canuto, C., Hussaini, M. Y., Quarteroni, A. & Zang, T. A. 1987 *Spectral Methods in Fluid Dynamics*. Springer, Berlin.

Darabi, J., Ohadi, M. M., Fanni, M. A., Dessiatoun, S. V. & Kedzierski, M. A. 1999 Effect of heating boundary conditions on pool boiling experiments. *HVAC&R Research* **5**, 1–14.

Deimling, K. 1985 *Nonlinear Functional Analysis*, Springer, Berlin.

Dhir, V. K. 1991 Nucleate and transition boiling heat transfer. *Int. J. Heat Fluid Flow*, **12**, 290–314.

Dhir, V. K. 1998 Boiling Heat Transfer. *Ann. Rev. Fluid Mech.* **30**, 365–401.

Govaerts, W. J. F 2000 *Numerical Methods for Bifurcations of Dynamical Equilibria*, SIAM, Philadelphia.

Gabaraev, B. A., Kovalev, S. A., Molochnikov, Yu. S., Solov'ev, S. L. & Usitakov, S. V. 2001 Rewetting and autowave change of boiling modes. *High Temp.*, **39**, 302–314.

Gurevich, A. V. & Mints, R. G. 1987 Self-heating in normal metals and superconductors. *Rev. Mod. Phys.* **59**, 941–999.

Janna, W. S. 1988 *Engineering Heat Transfer*. Van Nostrand Reinhold (international), London.

Kovalev, S. A. 1966 An investigation of minimum heat fluxes in pool boiling of water. *Int. J. Heat Mass Transfer*, **9**, 1219–1226.

Kovalev, S. A. & Rybchinskaya, G. B. 1978 Prediction of the stability of pool boiling heat transfer to finite disturbances. *Int. J. Heat Mass Transfer*, **21**, 691–700.

Kovalev, S. A. & Usitakov, S. V. 2003 Analysis of the stability of boiling modes involving the use of stability diagrams. *High Temp.*, **41**, 68–78.

Kreyszig, E. 1999 *Advanced Engineering Mathematics*, Wiley, Chichester.

Mudawar, I. 2001 Assessment of High-heat flux Thermal Management Schemes. *IEEE Transactions-CPMT: Components and Packaging Technologies*, **24**, 122–141.

Ott, E. 2002 *Chaos in Dynamical Systems*. Cambridge University Press, Cambridge (second edition).

Ouwekerk, H. van 1972 Burnout in pool boiling. The stability of boiling mechanisms. *Int. J. Heat Mass Transfer*, **15**, 25–33.

Speetjens, M. F. M. 2005 Steady-state behaviour of 2D pool boiling problems. In *Proceedings Eurotherm seminar 82 Numerical Heat Transfer* (ed. A. J. Nowak, R. A. Bialecki & G. Wecel).

Theofanous, T. G.. Tu, J. P., Dinh, A. T. & Dinh, T. N. 2002 The boiling crisis phenomenon. Part I: nucleation and nucleate boiling heat transfer. *Exp. Therm. Fluid Sci.*, **26**, 775–792.

Thome, J.R. 2003 Boiling. In *Handbook of Heat Transfer* (ed. A. Bejan & A. D. Krause), Wiley & Sons, Hoboken, pp 635-717.

Zhukov, S. A., Barelko, V. V. & Merzhanov, A. G. 1980 Wave processes on heat generating surfaces in pool boiling. *Int. J. Heat Mass Transfer*, **24**, 47–55.

Zhukov, S. A. & Barelko, V. V. 1983 Nonuniform steady states of the boiling process in the transition region between the nucleate and film regimes. *Int. J. Heat Mass Transfer*, **26**, 1121–1130.